Contents - S through Z

OPTICAL OBSERVATIONS OF THE COMET 2P/ENCKE DUST TRAIL. Yuki Sarugaku[1,2], Masateru Ishiguro[2], Naoya Miura[3], Fumihiko Usui[2], and Munetaka Ueno[3], [1]The Univ. of Tokyo, 7-3-1, Hongo, Bunkyo-ku, Tokyo, 113-0033, JAPAN. sarugaku@planeta.sci.isas.jaxa.jp, [2]ISAS/JAXA, 3-1-1, Yoshinodai, Sagamihara, Kanagawa, 229-8510, JAPAN, [3]The Univ. of Tokyo, 3-8-1, Komaba, Meguro-ku, Tokyo, 153-8902, JAPAN.

Introduction: Cometary dust trails were first detected by the Infrared Astronomical Satellite [1], [2]. They are composed of large dark particles, which are ejected at low velocities from the nuclei and extend along the orbits of the parent bodies. It is recently that trails were detected in visible wavelength [3], [4]. The scattered light is a basic but a new tool to study dust trails.

Observations: Comet 2P/Encke is a good target to study dust trails for following reasons: (1) the existence of the 2P/Encke trail was clearly identified by the previous studies [5], [6]; (2) it is possible to observe 2P/Encke in wide range of phase angle because the orbit crosses the Earth orbit (perihelion distance is 0.34 AU, aphelion distance is 4.10 AU).

We observed 2P/Encke 15 nights from 2002 September to 2004 September (perihelion passege of 2P/Encke was on 29 December 2003.). The observations were carried out using Kiso 1.05-m telescope (13 nights) and University of Hawaii 2.24-m telescope (2 nights). During these observations 2P/Encke was at heliocentric distance R of 0.70-3.98 AU, geocentric distance Δ of 0.26-2.97 AU, and phase angle α of 1-135°. When 2P/Encke closed to the Earth (Δ = 0.26-0.35 AU), the trail was not detected. On the contrary we could detect it when 2P/Encke was near aphelion (R = 3.98 AU, Δ = 2.97 AU).

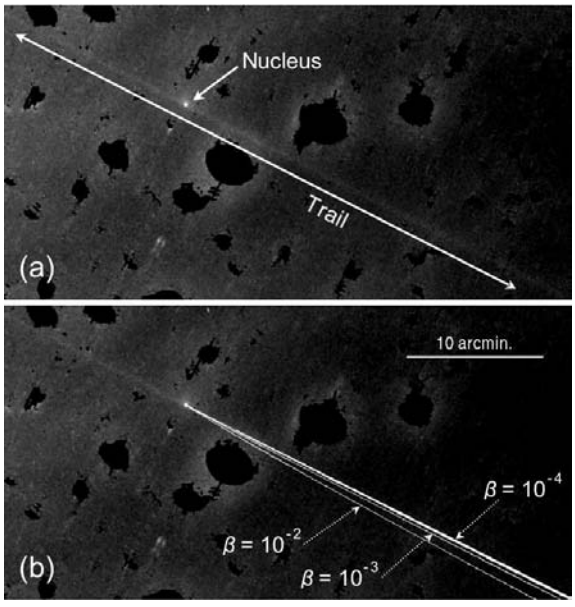

Figure 1: (a) Composite image of the 2P/Encke trail observed on 22 September 2003. Black spots have no value, which are made in the process of our data reduction to reduce contamination of stars. (b) Syndyne curves of $\beta = 10^{-2}, 10^{-3}$, and 10^{-4} are overlaid on fig. 1(a). The 2P/Encke trail agrees with syndyne curve of $\beta < 10^{-4}$.

Results: The 2P/Encke trail was detected at 5 different epochs. The range of R, Δ, and α of 2P/Encke, where the trail was detected, are 1.78-3.98 AU, 0.94-2.97 AU, and 1-26°, respectively (Table 1). According to fitting of the syndyne curves, we found that the trail is composed of particles whose size is larger than approximately 1 cm ($\beta < 10^{-4}$), which is consistent with the previous studies. In addition, it is likely that the intensity of scattered light increases at low phase angle by comparison of the data obtained at different phase angles.

Table 1: Observational summary. All observations were carried out with R band filter. Symbol ◯ shows that 2P/Encke trail was detected.

DATE (UT)	R (AU)	Δ (AU)	α (°)	TEL.	EXP. (min.)	TRAIL
2002/09/09	3.98	2.97	1	Kiso	72	◯
2003/09/22	1.78	0.94	24	Kiso	65	◯
2003/11/14	1.05	0.26	69	Kiso	86	–
2003/11/16	1.02	0.26	76	Kiso	40	–
2003/11/17	1.00	0.26	79	Kiso	67	–
2003/11/18	0.99	0.26	83	Kiso	73	–
2003/11/21	0.94	0.27	93	Kiso	58	–
2003/11/22	0.92	0.27	97	Kiso	67	–
2003/11/23	0.90	0.27	100	Kiso	53	–
2003/11/26	0.85	0.29	110	Kiso	48	–
2003/12/02	0.74	0.33	129	Kiso	26	–
2003/12/04	0.70	0.35	135	Kiso	16	–
2004/05/23	2.28	2.12	26	UH88	50	◯
2004/08/13	2.94	1.93	2	Kiso	55	◯
2004/09/09	3.12	2.25	11	UH88	42	◯

References: [1] Davies, J. K. et al. (1984) *Nature*, 309, 315-319. [2] Sykes, M. V. et al. (1986) *Science*, 232, 1115-1117. [3] Ishiguro, M. et al. (2002) *ApJ*, 572, L117-120. [4] Lowry, S. C. et al. (2003) *LPS XXXIV*, Abstract #2056, [5] Sykes, M. V. and Walker, R. G. (1992) *Icarus*, 95, 180-210, [6] Reach, W. T. et al. (2000) *Icarus*, 148, 80-94.

SUMMARY OF OBSERVATION OF INTERPLANETARY AND INTERSTELLAR DUST BY MARS DUST COUNTER ON BOARD NOZOMI. S. Sasaki[1], E. Igenbergs[2], H. Ohashi[3], R. Münzenmayer[2$], W. Naumann[2#], R. Senger[2], F. Fischer[4], A. Fujiwara[5], E. Grün[6], K. Nogami[7], I. Mann[8], H. Svedhem[9], [1] Mizusawa Astrogeodynamic Observatory, National Astronomical Observatory of Japan, 2-12 Hoshigaoka, Mizusawa, 023-0861, Japan (sho@miz.nao.ac.jp), [2] LRT, TU-München, 85748 Garching, Germany, [3] Tokyo University of Marine Science and Technology, Tokyo 108-0075, Japan, [4] RTSG, TU-München, 80333 München, Germany, [5] ISAS/JAXA, Sagamihara, 229-8510, Japan, [6] MPI-Kernphysik, 69117 Heidelberg, Germany, [7] Dokkyo University School of Medicine, Tochigi 312-0207, Japan, [8] Institut für Planetologie, Westfälische Wilhelms-Univ., 48149 Münster, Germany, [9] ESA-ESTEC, PO Box 299, 2200 AG Noordwijk, The Netherlands, [$] Now at Astrium Space, Postfach 1420, 88039 Friedrichshafen, Germany, [#] Now at Kayser-Threde GmbH, 81379 München, Germany.

Introduction:

Mars Dust Counter (MDC) is a dust detector of impact ionization type on board Japanese Mars mission NOZOMI. Although its weight is only 730g, MDC can determine mass, velocity, and direction of a dust particle using rise time of impact-induced charge signals [1]. The main objective of MDC is to discover the predicted martian dust ring or torus [2]. Dust abundance detectable by NOZOMI-MDC was predicted under the self-sustaining mechanism, where satellite-dust collisions are the main dust source [3].

Due to a problem at the powered fly-by with the Earth on December 1998, NOZOMI orbital plan was changed. From December 1998 to December 2002, NOZOMI takes an eccentric orbit whose perihelion and aphelion are at the Earth's orbit and at the Mars' orbit, respectively. Then, after two flybys with the Earth in December 2002 and June 2003, NOZOMI approached Mars in December 2003. NOZOMI would have observed circummartian environment by highly elliptic orbits around Mars from 2004. However, NOZOMI did not recover from electronic trouble which occurred in April 2002. Insertion into circummartian orbit was finally given up in December 2003. MDC continued observation of interplanetary (and interstellar) dust by April 2002. Here we summarize dust observation of MDC.

Dust detection:

After the launch on 4th, NOZOMI took eccentric parking orbits around the Earth for five months performing two fly-bys with the moon. MDC has detected more than 20 impact during the circumterrestiral orbit. During encounter with Leonids meteor stream, MDC detected a couple of high-velocity dust particles but their direction differed from meteor stream dust. From 1999, NOZOMI entered the cruising phase. Particles with impact velocities smaller than 4km/s have not been detected in the cruising phase. On the contrary, high velocity particles (v>40km/s) are detected only during the cruising phase, especially in 1999.

Impact data in the cruising phase are shown in Figs. 1 nd 2. Impact events in 1999 are shown in Figs. 1. Most of dust particles are Keplerian dust particles moving around the sun. There are several high velocity particles which are apparently different from such Keplerian particles, although there is direction ambiguity of ±several tens degree because of the large aperture of MDC sensor. In Fig. 1 (b), direction of two dust particles (**b**, **e**) corresponds to that of typical interstellar particles, which should correspond to the direction of the solar system moving against the surrounding interstellar gas cloud with a relative velocity 26km/s [4]. Particle **a** has a large vertical component. Other high-velocity particles **c**, **d** would have different origin but the component with this direction has not been reported in the interstellar dust source [5].

In 2000-2001 season, MDC detected similar number of dust particles but fewer high velocity particles (Fig. 2(a)) compared with those in 1999. Figure 2(b) shows that there is only one candidate **f** of interstellar dust. Most of particles are typical interplanetary dust particles moving around the sun. The difference between 1999 data and 2000-2001 data does not necessarily mean the change of interstellar dust flow. It could be rather explained by the change of dust detection efficiency according to NOZOMI spin axis direction.

In summary, MDC detected more than 100 dust particles in space. Not only Keplerian dust particles but also interstellar dust particle candidates were detected by MDC.

References: [1] Igenbergs, E., Sasaki, S., et al., *Earth Planets Space* **50**, 241-245, 1998. [2] Sasaki, S., *Adv. in Space Res.* **23**, 1907-1910, 1999. [3] Sasaki, S., *In Physics, Chemistry, and Dynamics of Interplanetary Dust*, ASP Conf. Ser. **104**, 187-190, 1996. [4] Grün, E.,et al., *Astron. Astrophys.* **286**, 915-924, 1994. [5] Taylor, A. et al., *Nature* **380**, 323-325, 1996.

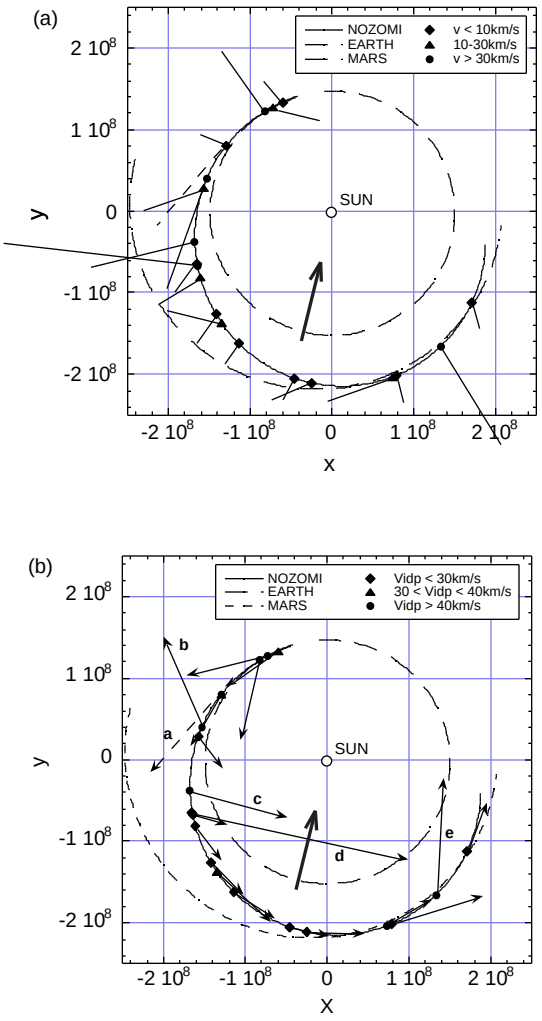

Fig. 1 Dust particle impacts detected by MDC in 1999. Orbits of NOZOMI, the Earth, and Mars are shown in the ecliptic plane. The +x direction is the direction of the Sun at vernal equinox. An arrow toward the sun denotes the direction of interstellar gas flow into the solar system. (a) Direction of MDC sensor aperture and impact velocity (i.e. relative velocity between NOZOMI and a dust particle). For each impact, direction is expressed by a line from the impact mark. The length of each line corresponds to velocity of the impacted particle. One event with a broken line denotes a fast impact with a large vertical velocity component. (b) Velocity of dust in the interplanetary space calculated from impact velocity and orbital velocity. Dust particles with high velocity (>40km/s) are denoted by attached characters (**a**, **b**, **c**, **d**, **e**).

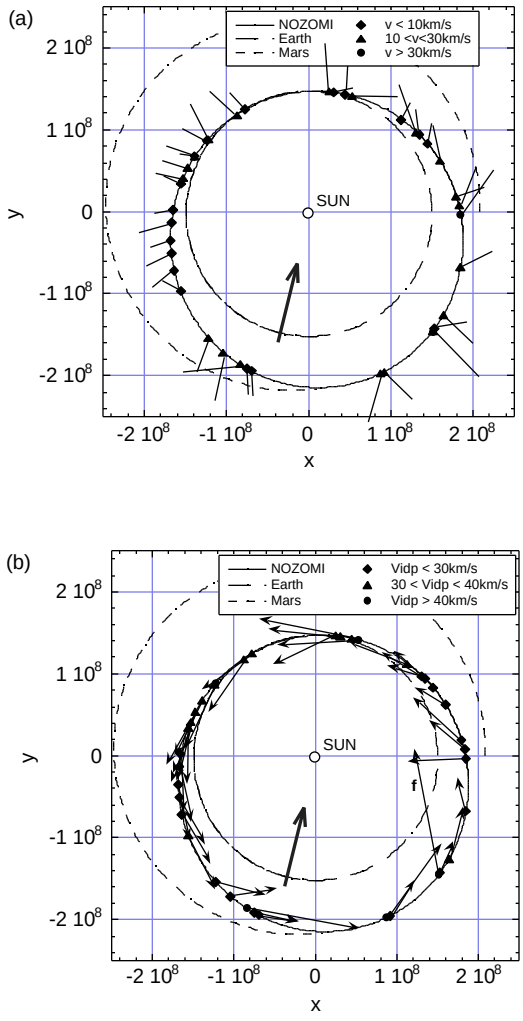

Fig. 2 Dust particle impacts detected by MDC in 2000 and 2001. Legends and figure formats are the same as Fig.2. (a) Direction of MDC sensor aperture and impact velocity. (b) Velocity of dust in the interplanetary space calculated from impact velocity and orbital velocity. A dust particle with high velocity is denoted by attached characters (**f**).

UPDATES ON THE DUSTY RINGS OF JUPITER, URANUS AND NEPTUNE. M. R. Showalter[1], J. A. Burns[2], I. de Pater[3], D. P. Hamilton[4], J. J. Lissauer[5], and G. Verbanac[6], [1]SETI Institute (515 Whisman Road, Mountain View, CA 94043, mshowalter@seti.org), [2]Cornell University (328 Space Sciences Bldg., Ithaca, NY 14853, jab16@cornell.edu), [3]U. C. Berkeley (601 Campbell Hall, Berkeley, CA 94720, imke@astron.berkeley.edu) [4]U. Maryland (Dept. of Astronomy, College Park MD 20742, hamilton@astro.umd .edu), [5]NASA Ames Research Center (M.S. 245-3, Moffett Field, CA 94035-1000, jlissauer@mail.arc.nasa.gov), [5]Geophysical Institute "Andrija Mohorovicic" (Horvatovac bb, 10000 Zagreb, Croatia, verbanac@irb.hr).

Introduction: We present recent results from observing the ring systems of Jupiter, Uranus and Neptune, using the Hubble Space Telescope (HST) in the visual and the 10-meter W. M. Keck Telescope in the infrared. Using Earth's most powerful telescopes, we find that all three ring systems are revealing new and unexpected properties.

Neptune: HST images taken November 2004 to June 2005 have revealed the ring-arcs of Neptune in visual light for the first time since the Voyager flyby of 1989 (Fig. 1). By operating at wavelengths similar to that of Voyager's cameras, we determine that the trailing arcs Egalité and Fraternité show no significant absolute change in brightness over the last 16 years, contradicting earlier suggestions. However the leading arcs Courage and Liberté have nearly vanished, confirming the continuation of trends noted in recent Earth-based infrared detections. The inner Leverrier ring is also detectable in the new HST data. Initial analysis indicates that it is several times brighter than in the Voyager images; this preliminary result requires further investigation.

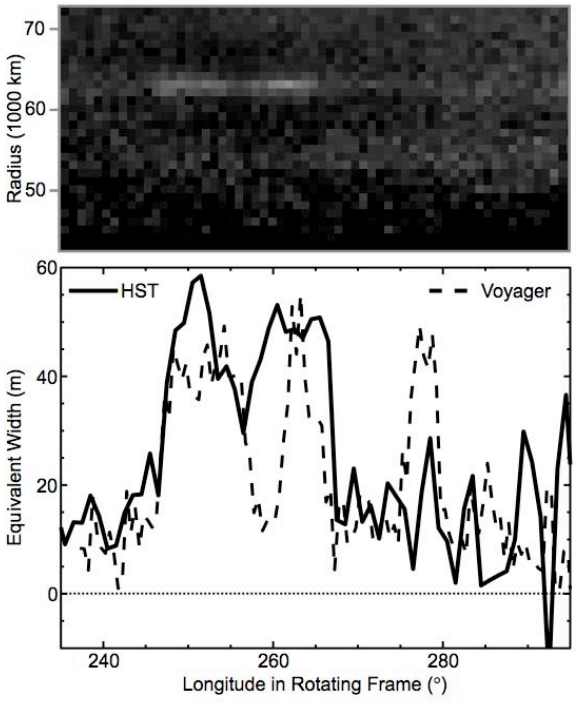

Fig. 1. Arc image and profile compared to Voyager.

This same data set has also recovered all the inner moons of Neptune except tiny Naiad; our data should be sufficiently sensitive to detect Naiad and we attribute its non-detection so far to the large uncertainty in this moon's ephemeris.

Jupiter: Our studies of the three components of Jupiter's ring system incorporate a reanalysis of Galileo and Voyager data in addition to the newer Earth-based data sets.

Gossamer Rings. This system consists of two overlapping rings, one bounded by Amalthea and the other by Thebe. The rings are superficially consistent with the model of Burns et al. [1], in which dust is ejected from each moon and evolves inward under Poynting-Robertson (PR) drag. We confirm that the ring thicknesses vary in proportion to radius, as one would expect if orbital inclinations are conserved. However both rings, and especially the Thebe ring, show signs that inclinations get somewhat randomized about their mean values during the dust's journey inward. Both rings also show a distinct peak in density just inward from their source moons, followed by a more uniform density downward to the main ring. The uniform regions are consistent with the PR drag model, but the peaks require a different explanation. The peak in Amalthea's ring is associated with material trapped in the plane of Amalthea's inclined orbit, indicating a population of dust whose nodes are locked. How Amalthea maintains this population is unclear. It is possible that the outer peak in Thebe's ring shows a similar morphology; the data are insufficient to say for certain.

We have performed detailed photometry of the Amalthea ring for the first time. Observations from HST, Keck, Galileo and Voyager are all consistent with a relatively flat power law size distribution of dust, of the form $n(r) \sim r^{-q}$, where q = 2–2.5. This is very similar to the size distribution in the main ring and is consistent with collisional ejecta evolving inward under a drag force. The ring's phase curve in backscatter is nearly flat, requiring that the dust grains be highly non-spherical.

Main Ring. In backscattered light, the ring shows a sharp increase in brightness between the orbits of Metis and Adrastea. This peak is not present in high-phase Galileo images, suggesting that this region contains a large population of macroscopic bodies bounded by the two moons. These macroscopic bodies, in addition to the two moons, are likely to serve as the primary parent bodies for the ring's prominent dust. Interior to the orbit of Metis the ring's profile in forward- and backscattered light appears similar, suggesting that dust is the primary component of this region.

One set of high-phase images from Galileo shows a series of vertical "ripples" in the ring (Fig. 2). The vertical amplitude is of order 1 km and the radial wavelength is irregular but typically ~ 1000 km. A density wave cannot be sustained in this low-mass ring; we propose that the vertical distortions may arise from an unseen population of smaller moons on slightly inclined orbits.

Halo. The inner halo is observed both in Galileo images at high phase and in Keck images at low phase. Both consistently show an inner limit of 100,000 km, a sharp concentration within a few thousand km of the ring plane, but with faint material still visible tens of thousands of km above and below.

Two competing models have been invoked to explain the halo. Schaffer and Burns [2] propose that PR drag draws dust inward from the source region, where it encounters Lorentz resonances that produce the large increases in thickness. Horanyi and Cravens [3] propose that grains evolve under "gyrophase drift" (GD), in which electric charges on the dust grains vary with orbital radius, causing the grains to spiral inward rapidly. In this scenario, Lorentz resonances play no explicit role.

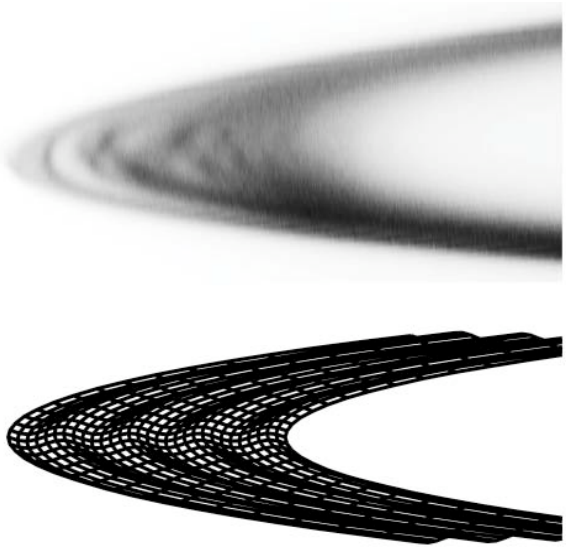

Fig. 2. A contrast-enhance negative of Galileo image 3689741.39 shows brightness variations across the ring ansa. A simple wire-frame diagram illustrates how these variations can be caused by vertical distortions of the ring plane.

Images of the main ring and halo pose a serious challenge to the GD model. This process admits a constant of the motion, the Jacobi integral, which involves only the orbital semimajor axis a and eccentricity e. As particles drift inward their eccentricities must grow, yielding a net increase in their apocenter radii. If the halo's sources lie in the main ring, then this process should be visible as an outward extension beyond the main ring's tip. Close examination of the finest-resolution images from Galileo, HST and Keck *exclude* the existence of this outward extension. The only material outside the main ring is from the gossamer rings; additional equatorial material cannot be brighter than ~ 1% of the main ring, which is incompatible with the much larger amount of material in the halo.

Uranus: Ongoing HST observations of Uranus span July 2003 to June 2006, during which the ring opening angle decreases from 18° to 3°. We have obtained repeated images spanning phase angles 0–3° and wavelengths 0.33 to 0.82 μm. All 9 of the brightest rings are resolved except the close inner set of Rings 6, 5 and 4. This data set has already yielded the discovery of two moons [4] too small to have been imaged by Voyager. We also detect longitudinally variable structures in several rings, most of which are related to known resonant perturbations and modes. We are employing photometric modeling to better define the dust content of these rings. We will also report on our attempts to detect the faint, dusty Ring λ. This work complements recent reports of secular changes in the Uranian dusty rings by de Pater et al. [5], based on Keck data in the infrared.

References: [1] Burns J. A. et al. (1999) *Science 284*, 1146–1150. [2] Schaffer L. and Burns J. A. (1996) *Icarus 96*, 65–84. [3] Horanyi M. and Cravens T. E. (1996) *Nature 381*, 293–295. [4] Showalter M. R. and Lissauer J. J. (2003) IAU Circular #8209. [5] de Pater, I. et al. (2005) *Icarus*, in press.

Acknowledgments: Partial support for this work was provided by NASA through grants GO-09823 and GO-10398 from the Space Telescope Science Institute, which is operated by the Association of Universities for Research in Astronomy, Inc., under NASA contract NAS5-26555.

E RING SOURCES — CASSINI FLYBYS WITH ENCELADUS

F. Spahn[1], N. Albers, V. Dikarev, T. Economu, E. Gruen, M. Hoerning, S. Kempf, A. V. Krivov, M. Makuch, J. Schmidt, M. Seiss, R. Srama, M. Sremcevic
[1]Institute of Physics, University Potsdam, D-14469 Potdam, Germany
(fspahn@agnld.uni-potdam.de)

Abstract

The satellite Enceladus is considered to be the main source of Saturn's E ring. Impactor-ejecta mechanisms are very likely the major processes to lift off particles from its surface. Nevertheless, it is still not clear what is the main impactor family causing the dust ejecta and whether other bodies in the E ring serve as additional sources. In order to distinguish the dust ejecta originating from potential sources (Enceladus and Tethys) from the bulk of the E ring we perform numerical particle experiments in order to simulate the fate of grains just ejected from Enceladus and Tethys. In this way we model the E ring configuration where the A ring, Enceladus and Tethys act as sinks and where Enceladus and Tethys are the only source. We found striking differences in the dust fluxes coming from the source satellites compared to the E ring background in the vicinity of the sources – this concerns both, the size distribution and also the impact rate expected at a dust detector. These can possibly be measured with the cosmic dust analyzer (CDA) or high rate detector (HRD) aboard the Cassini spacecraft. We compare these theoretical predictions with the HRD-data for certain Cassini flybys (E3, E4 and E11) with Enceladus and try to distinguish the freshly ejected material from the E ring background. Especially the E11 encounter provides the unique chance to measure the dust "cloud" around Enceladus – another strong hint for the impactor-ejecta mechanism as a dust generating process. We further found that Tethys contributes a considerable amount (30of the Enceladus contribution, depending on the impactor family) of dust to the E ring – a dust supply necessary to explain the large extent of that ring and also the additional density hump near the Tethys orbit seen in ground based observations (I. dePater).

CASSINI SATURN DUST MEASUREMENTS. R. Srama[1], M. Burton[4], S. Helfert[1,3], S. Kempf[1], G. Moragas-Klostermeyer[1], A. Mocker[1], F. Postberg[1], M. Roy[4], the CDA science team and E. Grün[1,2], [1]Max Planck Institute Nuclear Physics, Heidelberg, Germany, [2]HIGP, Univ. of Hawaii, Honolulu, Hawaii, USA, [3]Helfert Informatik, Mannheim, Germany, [4]JPL, Pasadena, USA.

Abstract The Cassini spacecraft is in orbit around Saturn since July 2004. During the first year, amazing discoveries of the dust environment at Saturn were achieved by the dust instrument onboard Cassini, the Cosmic Dust Analyzer (CDA)[1]. Here, an overview is given about the discoveries and achievements of CDA.

The approach to Saturn showed sporadic increases of the dust rate caused by tiny (few nano meter) and fast (>100 km s^{-1})particles ("nano-dust") which reached Cassini 100 million km away from Saturn. This discovery of Saturn's dust streams was further investigated by CDA during the first orbits and a detailed analysis has shown, that Saturn's A ring is partly responsible for this type of stream particles [2, 3].

In the saturnian system many grains carrying an electrical charge were detected by CDA. CDA has measured for the first time both, negative and positive charges of dust particles which are correlated to the distance to Saturn and to the local magnetosphere properties (compare [4]).

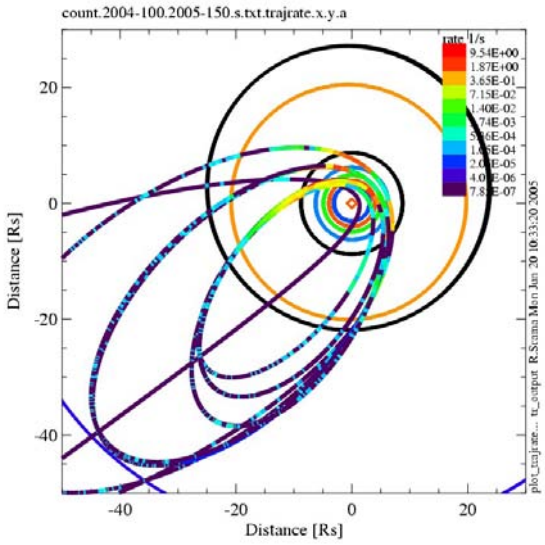

Fig. 1: The trajectory of Cassini, the orbit of the moons (from the outside to the inside: Hyperion, Titan, Rhea, Dione, Tethys, Enceladus), and the CDA dust event rate (color coded on the Cassini trajectory). The measured event rate is highly fragmented due to Cassini's pointing changes.

Saturn is surrounded by its optically faint E ring. CDA performed outstanding measurements of dust densities, particle size distributions and even particle compositions. This was possible due to the fact that an in-situ dust instrument like CDA is a factor of 1000 more sensitive to detect dust densities than an optical instrument. CDA confirmed that the particles are composed of micron sized, almost pure water ice particles.

Furthermore, it was shown, that Saturn's E ring is much more extended in both, the radial and the vertical dimensions (Fig. 1). Significant dust densities were detected as far as 16 Saturn radii away from Saturn.

A significant source of the E ring particles is the surface of the icy moon Enceladus, which is continuously bombarded by ring and interplanetary particles. The flyby of Cassini at Enceladus and crossings of the orbit of Enceladus lead to a strong increase of the particle density. In addition, the High Rate Detector (HRD) detected a clear population of dust particles bigger than 2 µm. Cassinis' flyby at Enceladus on day 195 in 2005 will shed light on the fundamental question, if Enceladus is the major source of the E ring particles [5].

References

[1] Srama R. et al. (2004) *SSR*, 114, 1-4, 465-518
[2] Kempf S. et al. (2005) *Nature*, 433, 7023, 289-291
[3] Kempf S. et al. (2005) *Science*, 307, 5713, 1274-1276
[4] Kempf S. et al. (2004) *Icarus*, 171, 317-335
[5] Spahn F. et al. (1999) *JGR*, 104, 2411-24120

Acknowledgements The Cosmic Dust Analyzer project is supported under the DLR grant 50OH0304.

A NEW LARGE AREA TOF MASS SPECTROMETER. R. Srama[1], M. Rachev[1], S. Helfert[1,3], S. Kempf[1], G. Moragas-Klostermeyer[1], A. Mocker[1], F. Postberg[1] and E. Grün[1,2], [1]Max Planck Institute Nuclear Physics, Heidelberg, Germany, [2]HIGP, Univ. of Hawaii, Honolulu, Hawaii, USA, [3]Helfert Informatik, Mannheim, Germany.

Abstract Based on experience with current space dust instruments on-board interplanetary missions, a novel Dust Telescope is being developed. A dust telescope is a combination of a dust trajectory sensor and a mass analyzer. The trajectory sensor is used to determine the speed, mass and trajectory of interplanetary and interstellar dust grains. In contrast, the mass analyzer provides the elemental composition of individual grains. Here, we report about the successful tests of the large area mass analyzer (LAMA) at the dust accelerator of the Max Planck Institute for Nuclear Physics in Heidelberg.

Instrument The flux of interplanetary and interstellar dust in the vicinity of the Earth can be as low as $1x10^{-5}$ s^{-1} m^{-2}. For this reason we developed a time-of-flight mass spectrometer with a sensitive area as big as 0.1 m^2. The lower limit for the required mass resolution was supposed to be 100. The result of the design study using the SIMION modeling package is a an instrument with a plane ring shaped target, an acceleration grid, a field free drift zone and a one-stage reflectron. The reflectron uses parabolic shaped grids in order to focus the ions, generated by the hyper-velocity impact of a micro meteoroid, onto a large ion detector (multi channel plate) (Fig. 1). The calculated mass resolution is above 150 for all impact positions and for a large variety of initial ion energies and ion emission angles in front of the target. The instrument employs an acceleration voltage of +5000 V.

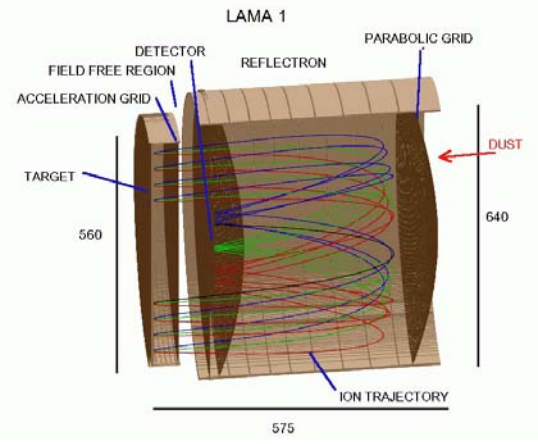

Fig. 1: Schematics of the Large Area Mass Analyzer. The dimensions are given in mm. The colored curves represent ion trajectories of different impact locations.

Measurements Initial test were performed with the laboratory model of LAMA at the dust accelerator facility in Heidelberg. Micron sized grains of iron and latex with impact speeds between 5 and 20 km s^{-1} were used to study the mass resolution of the instrument. Fig. 2 shows a typical spectrum achieved with iron projectiles and Fig. 3 shows a mass spectrum of a latex particle impact. Both spectra show very clearly the separation of adjacent mass lines even in the mass range above 100. A preliminary analysis revealed mass resolutions of up to 300. The first results therefore confirm the predicted mass resolutions of the SIMION calculations. The instrument concept was proven and is ready for a Cosmic DUNE mission.

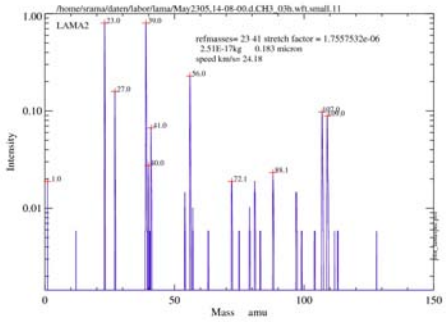

Fig. 2: Time-of-flight mass spectrum measured by LAMA. An iron particle with a speed of 24 km/s was shot onto the silver target.

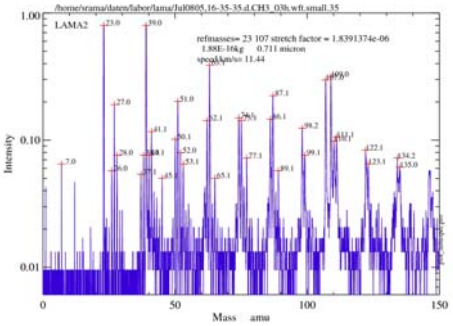

Fig. 3: LAMA mass spectrum of a latex particle with an impact speed of 11 km/s and a size of 0.7 µm. The target was silver. The impact process forms a variety of hydrocarbons which are well resolved by the spectrometer. The silver isotopes appears at 107 amu and 109 amu and are clearly separated.

Acknowledgments This research is supported by DLR grant 50OO0201.

TRAJECTORY SENSOR FOR SUB-MICRON SIZED DUST. R. Srama[1], A. Srowig[1,2], S. Helfert[1], S. Kempf[1], G. Moragas-Klostermeyer[1], S. Auer[3], D. Harris[4], E. Grün[1,4], [1]MPI-K, Heidelberg, Germany, [2]ASIC Lab. Univ. Heidelberg, Germany, [3]A&M Assoc., Basye, USA, [4]HIGP, Honolulu, USA.

Dust particles' trajectories are determined from the charges induced in sensor electrodes by charged dust grains. Based on experience with current space dust instruments [1] a novel Dust Trajectory Sensor has been developed. The Dust Trajectory Sensor will provide a ten times increased sensitivity of charge detection over Cassini's Dust Analyzer sensitivity [2] such that even in interplanetary space statistically significant numbers of dust trajectories can be obtained. The sensor measures dust charges $\geq 10^{-16}$ C and allows us to determine trajectories of submicron-sized grains with accuracies of ~1° in direction, and ~1% in speed.

A trajectory sensor has been set-up (Fig. 1) for dust accelerator tests. It consists of four sensor grids mounted between two electrical shielding grids [2]. Each sensor grid consists of 15 parallel wire electrodes (wires separated by 20 mm), each electrode being connected to a separate charge-sensitive amplifier (CSA). The wire directions of adjacent sensor grids are orthogonal. The distance between grid planes is 40 mm. Each pair of adjacent wire electrodes within a sensor grid acts as a one-dimensional position-sensitive detector: The wire that senses the highest induced charge is closest to the dust particle's trajectory. Neighboring wires sense lower charges. The ratios of charge amplitudes yield the exact coordinate of the grain's location of passage through that grid plane [3]. Accuracies of 0.1° in direction and 0.1% in speed have been demonstrated with dust particles from the Heidelberg dust accelerator facility [4].

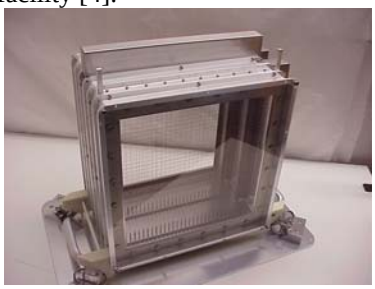

Fig. 1 Lab set-up of the dust trajectory sensor

Key elements of the trajectory sensor are the charge-sensitive amplifier (CSA) and the transient recorder. An Application Specific Integrated Circuit (ASIC) version (Fig. 2) was developed in cooperation with the Kirchhoff Institute for Physics of the Heidelberg University. It consist of two individual chips [5]. The front-end chip contains the CSA and a logarithmic amplifier for the compression of the dynamic range from 10^{-16} C to 10^{-13} C. Its rms noise performance is 1.5 10^{-17} C (100 electrons), in a bandwidth from 10 kHz to 10 MHz. The transient recorder chip has 32 channels of analog-digital converters with an accuracy of 10 bits at a 20 MHz sampling rate and 32 digital pipelines. A pipeline is a synchronous SRAM ring-buffer for 50 ms trigger latency. An external trigger signal (e.g. derived from the dust impact onto an impact detector placed behind the trajectory sensor) stops the recording and all data is serially readout.

First dust accelerator tests at the Max-Planck-Institute for Nuclear Physics have been performed with the described set-up. A network of 30 front end microchips and one transient recorder chip were integrated with the sensor. The tests were performed with iron particles with speeds up to 30 km/s (0.1 to 1 µm grain size) which demonstrate the expected performance.

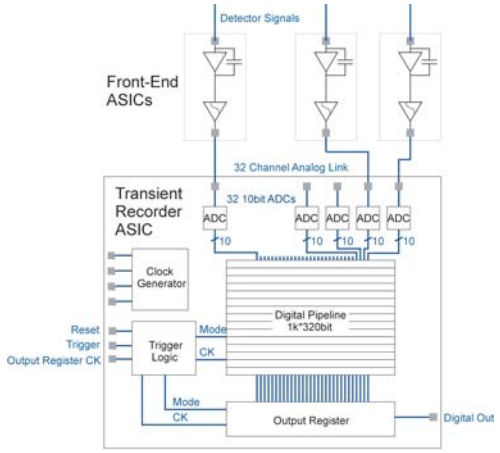

Fig.2 Block diagram of both the front-end and transient recorder ASICs

[1] Kempf, S., et al., 2004, Icarus, 171, 317-335. [2] Srama, R., et al., 2004b, ESA-SP 543, 73-78. [3] Auer S. and von Bun, F., 1994, in: Workshop on Particle Capture, Recovery, and Velocity/Trajectory Measurement Technologies (Zolensky M.E., ed.), LPI Tech. Rept. 94-05, Lunar and Planetary Institute, Houston, Texas, pp. 21-25. [4] Auer S., 1996, in: Physics, Chemistry, and Dynamics of Interplanetary Dust, ASP Conference Series, vol. 104, IAU Colloquium no. 150, Aug. 14-18, 1995, Gainesville, FL, pp. 251-254. [5] Srowig, A., 2004, PhD thesis, Heidelberg

Acknowledgements: This research is supported by NASA grant NAG5-11782 and by DLR grant 50OO0201.

TOF-SIMS ANALYSIS OF RESIDUES FROM ALLENDE PROJECTILES SHOT ONTO ALUMINUM FOIL – A STARDUST DRESS REHEARSAL. T. Stephan[1], J. Leitner[1], and F. Hörz[2], [1]Institut für Planetologie, Wilhelm-Klemm-Str. 10, 48149 Münster, Germany (stephan@uni.muenster.de), [2]NASA Johnson Space Center, Houston, Texas 77058, USA.

Introduction: Samples from the ongoing *Stardust* mission will offer the first opportunity to analyze cometary material that has been collected under controlled conditions at comet *81P/Wild 2* as well as contemporary interstellar dust [1, 2]. Furthermore, *Stardust* is the first sample return mission ever that will return material from a known object other than the Moon.

After return of the comet samples to Earth in January 2006, the primary goal will be to determine the elemental, isotopic, mineralogical, and organic composition of the dust and hence the properties of the cometary nucleus itself.

The *Stardust* mission will provide two different types of capture media containing cometary samples [2]. The primary sampling material is silica aerogel with density gradients varying from 5 to 50 mg/cm^3. It is used to decelerate impinging cometary grains with the least possible shock pressure during impact. In addition to 1039 cm^2 surface area of exposed aerogel, some 153 cm^2 of aluminum foils (Al 1100; >99 % pure) were exposed. These foils were primarily used to fix the aerogel cuboids and to facilitate their removal from the sample tray assembly.

Although even small cometary grains impacting on a metal foil at a velocity of 6.12 km/s are not expected to survive this process unaltered, the Al foil represents a valuable sampling material that might be the primary target material for small (sub-micrometer) or fluffy particles that disintegrate during penetration of the aerogel and that cannot be extracted easily from this highly porous and friable capture medium.

In this study, we used time-of-flight secondary ion mass spectrometry (TOF-SIMS) for the analysis of crater residues on Al foil from impact experiments using material from the Allende meteorite. The major goal of this study is to determine how well the chemical composition of Allende can be reproduced.

TOF-SIMS: The TOF-SIMS technique has been used for the analysis of extraterrestrial matter for more than a decade [3] including the analysis of impact residues from *LDEF* [4] and the *Hubble Space Telescope* solar array [5].

For the *Stardust* samples, TOF-SIMS has the unique opportunity to allow a comprehensive analysis with high lateral resolution and minute sample consumption [6]. During a typical analysis, less than one atomic monolayer is consumed while the sample is rastered with a ~0.2 µm Ga^+ primary ion beam. All secondary ions with a single polarity are detected quasi simultaneously after their passage through the time-of-flight spectrometer. Both polarities can be measured in two consecutive analyses. Elemental, isotopic, and molecular compositions are determined in parallel. Further analytical details are given in the literature [3].

Samples and Experimental Procedures: Powdered bulk material of 38–43 µm grain size of the CV3 chondrite Allende was shot onto Al foil at a velocity of 5.9 km/s. Based on the nominal projectile size, crater diameters as large as 180 µm are to be expected [7]. However, many individual grains fragmented during launch, resulting in a wide range of crater sizes.

In this study, four craters (#1–4) were selected for TOF-SIMS analysis. In the vicinity of crater #1, another crater (#1.1) and a Si-rich deposit without crater (#1.2) were chosen for further investigation. In the direct neighborhood of crater #4 also an additional crater (#4.1) was found that was treated separately. The following table comprises all samples investigated in this study.

sample	#1	#1.1	#1.2	#2	#3	#4	#4.1
size [µm]	120	7	9×5	100	40	18	4

All sample regions were analyzed after sputter cleaning by Ar ion bombardment. This cleaning became necessary since the entire Al foil was covered with a thin layer of mainly organic contaminants from the vaporized projectile sabot, which inhibited a proper analysis in the first place.

From the distribution of Mg, Si, Ca, and Fe, regions of interest were selected, and complete mass spectra were generated for these regions. After correction for Al foil blank, bulk element ratios were calculated using relative SIMS sensitivity factors obtained from glass standards that are usually used for quantitative TOF-SIMS analysis of silicates [3].

Results: Crater #1 does not show any residual material for a proper impactor characterization. However, all other sample regions exhibit enough material for quantitative analysis. Figure 1 shows lateral element distributions in the area of craters #4 and #4.1.

Quantitative results for all samples are summarized in Fig. 2: Element ratios normalized to Si show huge variations. Deposit #1.2 is clearly non-chondritic. Its Mg/Si-ratio is below 0.012×CV and also other major elements are more than a factor of 10 depleted compared to CV. Therefore, sample #1.2 was omitted for the calculation of average values. These average val-

ues are for most elements close to CV element ratios. Only three elements show deviations larger than a factor of two: Ca is enriched, Fe and Ni are depleted. However, a general element fractionation generated by the impact process cannot be deduced from the present data set.

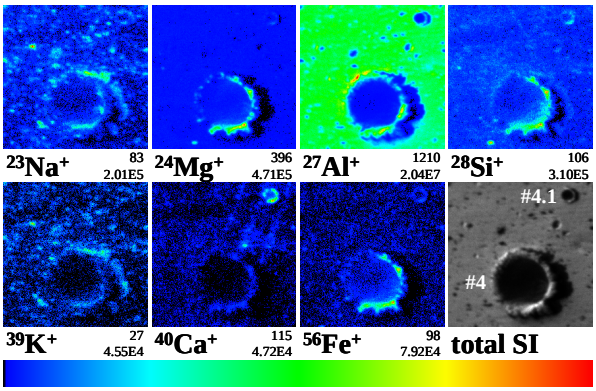

Fig. 1: TOF-SIMS secondary ion images showing two craters (#4 and #4.1) in Al foil. Field of view is 47×47 μm². All images use the same linear color scale normalized to the most intense pixel. Below each image, numbers for maximum and integrated intensities are given. A total positive secondary ion image is given in the lower left.

Since sputter cleaning was necessary prior to TOF-SIMS analysis, no useful information on organic constituents of the projectiles could be obtained. Usually organic compounds fragment during Ar bombardment. Typical silicone oil fragments as well as polycyclic aromatic hydrocarbons observed only before sputtering cannot be connected with the impact craters.

Contamination of the Al foil with Li, Be, B, C, and O prevents a quantitative analysis of these elements. Contamination with Na, Si, K, Sc, and V is responsible for some of the large error bars in Fig. 2, since blank subtraction had a major effect here. It is presently unknown, if this contamination is indigenous to the Al foil or if it results from the conditions during the impact experiments. Ar sputtering was not sufficient to remove this contamination completely.

Discussion: Although variations in element ratios from crater to crater are rather large, the average composition of all analyzed samples resembles remarkably well the expected element pattern. If compared with element ratios of different chondrite types [8], the TOF-SIMS data yield correlation coefficients above 0.95 for CV and CK, and below 0.95 for other carbonaceous chondrite classes. For L and LL ordinary chondrites, also correlation coefficients above 0.95 were found, mainly due to their low Fe and Ni concentrations. However, from the available data set, an unequivocal assignment to a specific chondrite class could not be made. Except for CH and EH chondrites, correlation coefficients are above 0.9 for all chondrite classes. For an unambiguous classification, data for light elements, especially C, would be crucial. It is hoped that the *Stardust* Al targets will be less contaminated with those elements.

The present results clearly indicate that chondritic projectiles impinging on Al foil at ~6 km/s can be identified by subsequent TOF-SIMS analysis of their residues. Further analyses will clarify, if deviations for Ca, Fe, and Ni are due to fractionation effects during impact or simply represent statistical variations in the inhomogeneous projectile material.

References: [1] Brownlee D. E. et al. (2003) *JGR, 108*, E8111. [2] Tsou P. et al. (2003) *JGR, 108*, E8113. [3] Stephan T. (2001) *Planet. Space Sci., 49*, 859–906. [4] Stephan T. et al. (1992) *LPS XXIII*, 1357–1358. [5] Stephan T. et al. (1995) *ESTEC Workshop on Space Debris on HST*, 25 pp. [6] Stephan T. (2003) *Workshop on Cometary Dust in Astrophysics, LPI Contrib. 1182*, 71. [7] Bernhard R. P. et al. (1994) *LPS XXV*, 107–108. [8] Lodders K. and Fegley B., Jr. (1998) *The Planetary Scientist's Companion.* Oxford University Press. 371 pp.

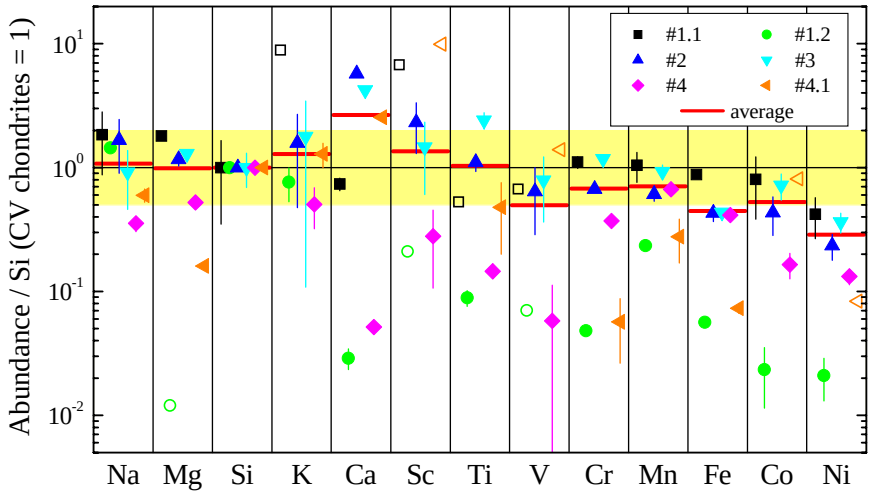

Fig. 2: Element ratios normalized to Si and CV chondrites show huge variations. Open symbols represent upper limits. Average values were calculated using all samples except #1.2, which is clearly non-chondritic. Most element ratios are within a factor of two (yellow area) CV-chondritic.

DEVELOPMENT OF THE LARGE AREA MASS ANALYZER. Z. Sternovsky[1], M. Horanyi[1], K. Amyx[1], S. Robertson[1], G. Bano[1], E. Gruen[2,3], R. Srama[2], S. Auer[4], [1]Laboratory for Atmospheric and Space Physics, University of Colorado, Boulder, CO, 80309 (Zoltan.Sternovsky@colorado.edu), [2] MPI-K, Heidelberg, Germany, [3] HIGP, Honolulu, USA, [4] A&M Assoc., Basye, USA

An instrument to analyze the chemical composition of dust particles in space is under development. Compared to similar previous instruments, such as the Galileo/Ulysses or Cassini dust detectors [1,2], this new instrument has a larger target area that makes it suitable for detecting interstellar dust particles. The device is a reflectron type time-of-flight mass spectrometer that measures the ions from the impact generated plasma due to hypervelocity dust impacts on solid surfaces. The mass spectrometer consists of the target, a single-stage reflectron potential configuration and an ion detector. The SIMION ion optics software package has been used to investigate different potential field configurations and optimize the mass resolution and focusing of the ions. The final configuration selected uses a set of six ring electrodes on the side and six annular electrodes at the top biased to different potentials to create the potential distribution of the reflectron. The annular target is of effective area approximately 0.2 m^2 and the mass resolution is m/dm ≈ 150. The target is biased to 5 kV and a grounded grid in front of the target is used to accelerate the ions. A microchannel plate is used as an ion detector. The laboratory model of the instrument has been fabricated and is undergoing preliminary testing. Dust impacts are simulated by using a frequency doubled (532 nm) Nd:YAG laser with ~8 ns pulse length. The laser can deliver up to 10 mJ of energy per pulse and its beam is focused to a ~ 15 micron spot size. The instrument will be calibrated at the Heidelberg dust acceleration facility.

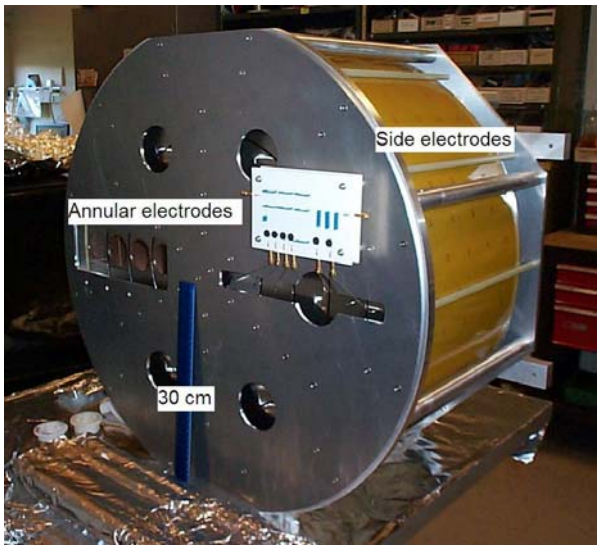

[1] Göller J. R. and Grün E. (1989) *Planet. Space Sci., 37*,1179-1206.

[2] Srama R., Ahrens T. J., Altobelli N., et al. (2004) *Space Sci. Rev. 114*, 465-518.

LUNAR SURFACE CHARGING: A GLOBAL PERSPECTIVE USING LUNAR PROSPECTOR DATA.

T. J. Stubbs[1], J. S. Halekas[2], W. M. Farrell[1], and R. R. Vondrak[1], [1]NASA Goddard Space Flight Center, Greenbelt, MD 20771, USA, [2]University of California, Berkeley, CA 94720, USA. Timothy.J.Stubbs.1@gsfc.nasa.gov.

Introduction: Our aim here is to use moments of the electron distribution function derived from Lunar Prospector Electron Reflectometer (LP/ER) data [1], together with basic probe equations [2], to determine the global variation in lunar surface electrostatic potentials for the different plasma environments encountered by the Moon. This will be a first step in better understanding and predicting global lunar surface charging under various conditions. This work will also include some simple estimates of the horizontal electric fields near the lunar terminator.

The surface of the Moon, like any object in a plasma, charges to an electrostatic potential that minimizes the total incident current [3]. The charging currents come from four sources: photoemission of electrons (J_{ph}), plasma electrons (J_e), plasma ions (J_i), and secondary electrons (J_{sec}). (J_{sec} arises primarily from surface ionization by plasma electrons.) The Moon is exposed to a variety of plasma environments during its orbit such that incident currents span several orders of magnitude. For about three-quarters of the time, the Moon is in the solar wind flow; otherwise, it is either in the tenuous plasma of the magnetospheric tail lobes, or the turbulent and energetic plasmas encountered in the geomagnetic plasma sheet and magnetosheath.

The lunar dayside typically charges positive, since J_{ph} usually dominates (see Fig. 1). As a result a "photoelectron sheath" forms above the surface, which in the solar wind extends ~1m, and effectively shields the charged surface from the surrounding plasma [4]. On the nightside, the lunar surface usually charges negative since J_e typically dominates. In this case a "Debye sheath" shields the surface potential [5] and can extend from meters to possibly ~1km [6]. There are significant uncertainties in current estimates of lunar surface potentials and almost nothing is known about their spatial distribution and temporal variation.

Implications: Surface charging processes are thought to drive the transport of lunar dust grains with radii <10μm, particularly near the terminator. The Surveyor landers observed ≈5μm grains levitating ~10cm above the surface [7,8]. During the Apollo missions 0.1μm-scale dust in the lunar exosphere was observed up to ~100km altitude [9,10,11]. The most viable mechanisms proposed to explain these observations have been based on the principle that the like-charged surface and dust grains act to repel each other such that dust is ejected from the surface. Under certain conditions, the heavier grains are predicted to electrostatically levitate near the surface [5,12], while the smaller grains are electrostically "lofted" to ~10km in altitude [13,14]. These phenomena could present a significant hazard to future robotic and human exploration of the Moon [15,16].

Spacecraft and Instrumentation: The LP spacecraft was in a rapidly precessing polar orbit about the Moon (period ~2 hours), which gave full coverage of the lunar surface twice every lunation. LP collected data for 18 months, with its altitude varying between 20 and 115 km, thus providing good coverage under most conditions. ER data is used to calculate electron concentrations (n_e) and temperatures (T_e) from kappa fits to the electron distribution functions [1]. As there is no ion data from LP we assume that the plasma near the Moon is quasi-neutral and the electrons and ions have the same temperature, i.e., $n_i = n_e$ and $T_i = T_e$.

Surface Charging Model: We calculate the electrostatic surface potential, ϕ_S, using the method and equations given in [2]. We solve numerically to find ϕ_S such that the net incident current is approximately zero, i.e., $J_e + J_i + J_{ph} \approx 0$. ($J_{sec}$ is not included here since on the dayside and near the terminator it is expected to be

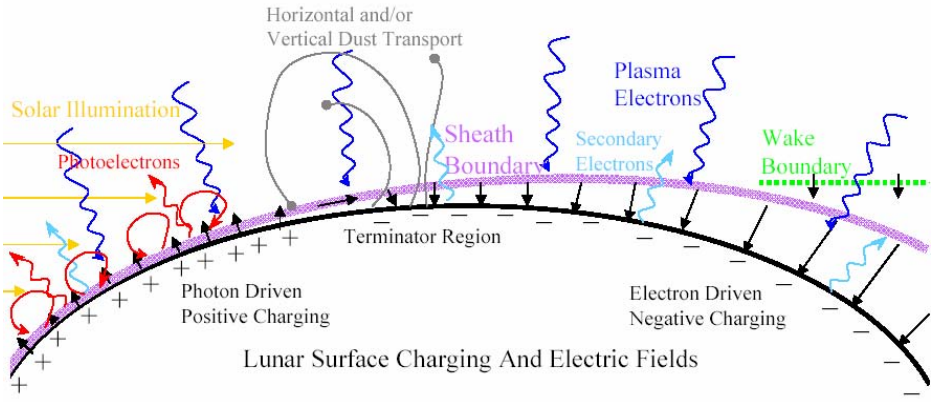

Fig. 1. Schematic of lunar electrostatic environment, showing charging current sources, surface charge, and electric fields (not to scale).

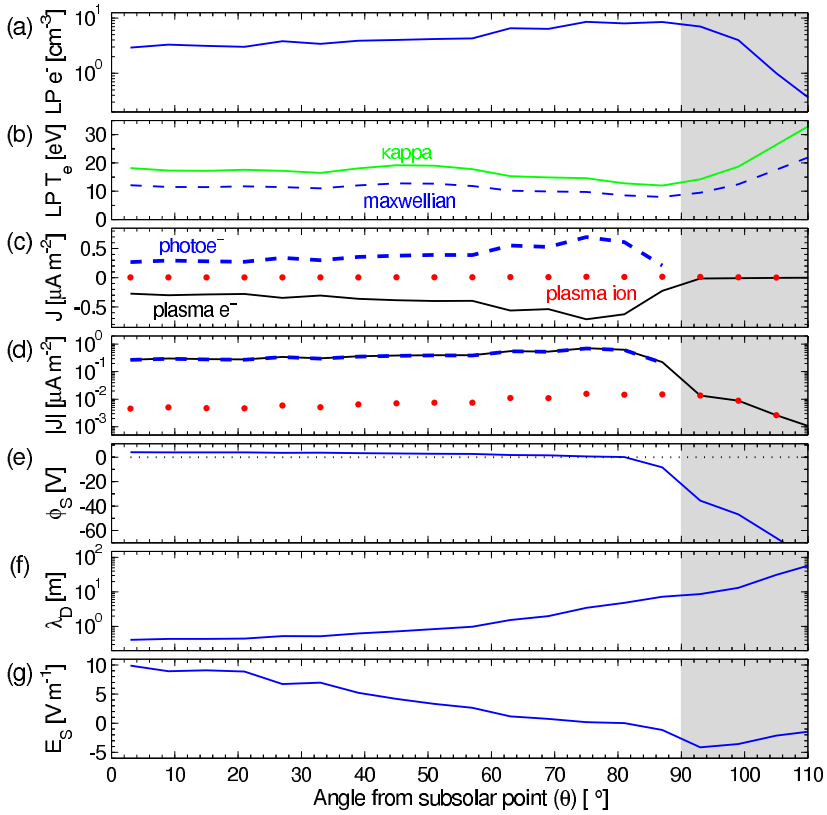

Fig. 2. Lunar surface charging predictions under typical solar wind conditions plotted as a function of angle from the subsolar point (θ). Input data: LP/ER derived electron (a) concentrations and (b) kappa (solid line) and maxwellian (broken line) temperatures. Current contributions from J_e (broken line), J_i (dots) and J_{ph} (solid line) shown on (c) linear and (d) log scales. (e) Lunar surface potential, ϕ_S, (f) Debye length of attracted species, λ_D, and (g) Surface electric field, E_S.

less significant than either J_e, J_i or J_{ph}.) The current density equations are different for positive ($\phi_S > 0$) and negative ($\phi_S < 0$) surface potentials [14]. Photocurrent density from normally incident sunlight is assumed to be 4.0×10^{-6} A m^{-2} [17] (given a surface photoelectron efficiency of 0.1). J_{ph} varies with the angle from the subsolar point, θ, and so is highest at the equator at local noon ($\theta = 0°$) and drops off to zero at the terminator ($\theta = 90°$). The Debye lengths used in this model are for the species attracted to the surface (e.g., where $\phi_S > 0$ we use the electron Debye length). It is important to note that the dominant source of electrons on the lunar dayside is from photoemission (at ~500 cm^{-3} this is ~100 times greater than in the solar wind). Assuming 1-D Debye shielding above a plane, the lunar surface electric field is given by $E_S = \phi_S / \lambda_D$.

Initial Predictions: Fig. 2 shows predictions for lunar surface charging given typical solar wind conditions. As expected the dayside is photo-driven ($\phi_S > 0$) and the nightside is electron-driven ($\phi_S < 0$). Due to the lower plasma concentrations, the nightside currents are much weaker.

In Fig. 2 we have only considered the vertical component of E_S. Horizontal electric fields will form between regions of different potential, and we would expect this to be most significant near the transition from $\phi_S > 0$ to $\phi_S < 0$ (i.e., near the terminator). We will make zeroth order estimates of horizontal E_S using a similar method to that described above. This could explain the enhancement in horizontal dust transport observed in-situ by the Apollo 17 LEAM experiment near the terminators [18,19].

References: [1] Halekas, J.S., et al. (2002) Geophys. Res. Lett., 2001GL014428. [2] Manka, R.H. (1973) Photon & Particle Interactions with Surfaces in Space, 347. [3] Whipple, E.C. (1977) J. Geophys. Res., 1525. [4] Singer, S.F. and Walker, E.H. (1962) Icarus, 1, 7. [5] Nitter, T. et al. (1998) J. Geophys. Res., 6605. [6] Halekas, J.S., et al. (2003) Geophys. Res. Lett., 2003GL018421. [7] Criswell, D.R. (1973) Photon & Particle Interactions with Surfaces in Space, 545. [8] Rennilson, J.J. and Criswell, D.R. (1974) The Moon, 10, 121. [9] McCoy, J.E. and Criswell, D.R. (1974) Proc. Lunar Sci. Conf. 5th, 2991. [10] McCoy, J.E. (1976) Proc. Lunar Sci. Conf. 7th, 1087. [11] Zook, H.A. and McCoy, J.E. (1991) Geophys. Res. Lett., 18, 2117. [12] Sickafoose, A.A. et al. (2002) J. Geophys. Res. 2002JA009347. [13] Stubbs, T.J., et al. (2005) Adv. Space Res., in press. [14] Stubbs, T.J., et al. (2005) Lunar Planet. Sci. Conf. 36th, 1899. [15] NASA Robotic and Human Lunar Exploration Strategic Roadmap (2005). [16] Stubbs, T.J., et al. (2005) Lunar Planet. Sci. Conf. 36th, 2277. [17] Goertz, C.K. (1989) Rev. Geophys., 27, 271. [18] Berg, O.E., et al. (1976) Interplanetary Dust and Zodiacal Light, 233. [19] Berg, O.E. (1978) Earth Planet. Sci. Lett., 39, 377.

IMPACT OF LUNAR DUST ON SPACE EXPLORATION. T. J. Stubbs, R. R. Vondrak and W. M. Farrell, NASA Goddard Space Flight Center, Greenbelt, MD 20771, USA, Timothy.J.Stubbs@gsfc.nasa.gov.

Introduction: From the Apollo era it is known that dust on the Moon can cause serious problems for exploration activities. Such problems include adhering to clothing and equipment, reducing external visibility on landings, and causing difficulty to breathing and vision within the spacecraft [e.g. 1,2]. An important step in dealing with dust-related problems is to understand how dust grains behave in the lunar environment.

Past Experiences. All astronauts who walked on the Moon reported difficulties with lunar dust. Eugene Cernan, commander of Apollo 17, stated that "… one of the most aggravating, restricting facets of lunar surface exploration is the dust and its adherence to everything no matter what kind of material, whether it be skin, suit material, metal, no matter what it be and it's restrictive friction-like action to everything it gets on" [1].

Highest Future Priority. NASA's Requirements for Lunar Exploration Program (RLEP) Document (ESMD-RQ-0014) states that the RLEP shall investigate the potential biological impacts of the lunar environment, including the micrometeoroid and dust environments (RLEP-M20 and RLEP-T20) [3]. Dust has also been highlighted as a priority by the Mars Exploration Program Assessment Group (MEPAG): "1A. Characterize both aeolian dust and particulates that would be kicked up from the martian regolith by surface operations of a human mission with fidelity sufficient to establish credible engineering simulation labs and/or software codes on Earth."

We shall briefly describe the properties of lunar dust and its impact on the Apollo astronauts, and then summarize three main problems areas for understanding its behavior: (1) Dust Adhesion and Abrasion, (2) Surface Electric Fields and (3) Dust Transport. These issues are all inter-related and must be well understood in order to minimize the impact of dust on future robotic and human exploration of the Moon.

Properties of Lunar Dust: Lunar dust was found to be similar to fine-grained slag or terrestrial volcanic ash [3].

Grain Size. With an average grain radius of ≈70μm, most dust is too fine to see with the human eye. 10–20% of dust has a radius <20μm [3].

Grain Shape. Dust grain shapes are highly variable and can range from spherical to extremely angular. Although, in general, grains are somewhat elongated [4].

Grain Conductivity. Lunar dust has low conductivity, and so can hold charge. However, conductivity can increase with: surface temperature; Infra-red (IR) light by ~10; and Ultra-violet (UV) light by ~10^6 [4].

Dust Impact on Astronauts:

Reduced Visibility. Exterior to the Lunar Module (LM) dust was kicked-up during landings which significantly reduced visibility [2]. Interior to the LM, dust would be brought in after moonwalks. It was reported by Alan Bean on Apollo 12 that "After lunar liftoff … a great quantity of dust floated free within the cabin. This made breathing without a helmet difficult, and enough particles were present in the cabin atmosphere to affect our vision" [2].

Respiratory. As mentioned, dust can make breathing difficult. It is very possible that chronic respiratory problems could arise in astronauts due to micro-scopic particulates in the lungs, especially after prolonged periods on the lunar surface [5].

Dust Adhesion and Abrasion:

Dust on Spacesuits. Alan Bean also noted that "… dust tends to rub deeper into the garment than to brush off" [2]. Dust adhered to spacesuits both mechanically and electrostatically. Mechanical adhesion was due to the barbed shapes of the dust grains, which allowed them to work into the fabric. Electrostatic adhesion was caused by charging of objects by the solar wind plasma and photo-ionization (see below). The abrasive effect of adhered dust can wear through the fabric of a spacesuit, drastically reducing its useful lifetime [1,2].

Dust on Lunar Surface Apparatus. Problems were experienced during Lunar Roving Vehicle (LRV) excursions, with much dust being kicked-up and covering exposed areas [1,4], leading to increased friction at mechanical surfaces. The resulting abrasive effect of dust increased wear and tear, which limited the lifetime of surface equipment.

From the recovery and examination of parts from Surveyor 3 during Apollo 12, it was found that dust accumulation and adhesion were heavier than anticipated [4] on both aluminum and painted surfaces.

Surface Electric Fields:

Lunar Surface Charging. Probe equations can be used to determine incident electric current densities on the Moon's surface, which can be used to find the surface electrostatic potential [6]. Using this approach it can be shown that the lunar dayside charges positive, as photo-electron currents dominate; and the lunar nightside charges negative, since plasma electron currents dominate. It is also possible for the transition from positive to negative surface potential to occur dayside of terminator [7].

Inclusion of Wake Physics. A wake or "void" forms downstream of the Moon when it is immersed in the solar wind flow [8]. This complicated interaction creates large electric potentials in the wake which leads to the formation of ion beams [9], and large electric fields at the terminators [8], amongst other phenomena.

Lunar Dust Transport:

In-situ Evidence for Transport of Charged Dust. Data from the Apollo 17 Lunar Ejecta and Micrometeoroids (LEAM) experiment was dominated by low energy impacts from electrostatically charged dust [10]. The peaks in the counts registered occurred around the terminators.

Evidence for Dust Above the Lunar Surface. Horizon glow (HG) and "streamers" from forward scattered sunlight were observed above the terminator by both surface landers and astronauts [e.g., 11,12]. It was suggested that near-surface HG (<1m) was caused by scattering from levitating dust grains with radii of ~5μm. This was due to electrostatic charging of the lunar surface and dust grains by the solar wind plasma and photo-ionization by solar UV and X-rays [6], which caused the dust to be repelled from the like-charged surface [e.g., 11,12,13]. Note that HG was ~10^7 too bright to be explained by micrometeoroid-generated ejecta [12,13].

There was also evidence for 0.1μm-scale lunar dust present sporadically at much higher-altitudes (~ 100km) [14]. The scale height for this dust population was determined to be ~10 km, which is too short to be caused by Na or K gas in the lunar exosphere [15]. Also, observations of these gases have been too dim to be seen by the unaided human eye [15].

It has been suggested that dust observed at high-altitudes is electrostatically "lofted" by the "dynamic dust fountain" effect [7], as opposed to static levitation mechanism used to explain heavier grains nearer the surface [12,13]. In the dynamic dust fountain model charged dust grains follow ballistic trajectories, subsequent to being accelerated upwards through a narrow sheath region by the surface electric field. These dust grains could affect the optical quality of the lunar environment for astronomical observations and interfere with exploration activities [e.g., 16].

References: [1] Goodwin R. (2002) Apollo 17 – The NASA Mission Reports: Vol. 1. [2] Bean, A.L. et al. (1970) Apollo 12 Preliminary Science Report, 29, NASA SP-235. [3] Robotic and Human Lunar Exploration Strategic Roadmap (2005). [4] Heiken, G.H., et al. (1991), Lunar Sourcebook a User's Guide to the Moon. [5] Biological Effect of Lunar Dust Workshop, NASA/ARC, March 29-31 (2005). [6] Manka, R.H. (1973) Photon & Particle Interactions with Surfaces in Space, 347. [7] Stubbs, T.J., et al. (2005) Adv. Space Res., in press. [8] Farrell, W.M. et al. (1998) Geophys. Res. Lett., 103, 23,653. [9] Ogilvie, K.W. et al. (1996) Geophys. Res. Lett., 23, 1255. [10] Berg, O.E., et al. (1976) Interplanetary Dust and Zodiacal Light, 233. [11] McCoy, J.E. (1976) Proc. Lunar Sci. Conf. 7th, 1087. [12] Rennilson, J.J. and Criswell, D.R. (1974) The Moon, 10, 121. [13] Criswell, D.R. (1973) Photon & Particle Interactions with Surfaces in Space, 545. [14] McCoy, J.E. and Criswell, D.R. (1974) Proc. Lunar Sci. Conf. 5th, 2991. [15] Zook, H.A. and McCoy, J.E. (1991) Geophys. Res. Lett., 18, 11, 2117. [16] Murphy, D.L. and Vondrak, R.R. (1993) Proc. Lunar Planet. Sci. Conf. 24th, 1033.

Lunar Exploration Issues	→ Connection →	Space Science Expertise
Dust Adhesion	Determining how charged particulates in a plasma interact with a surface.	Surface physics Plasma surface interactions, e.g. sputtering
Surface Electric Fields	Understanding how large objects charge in a plasma and under UV & X-rays.	Spacecraft charging Probe physics Wake physics
Dust Transport	Understanding how particulates immersed in a plasma interact with it. Knowing how the dust and plasma are modified by this interaction.	Dusty plasma physics Planetary Rings
Surface Composition	Understanding the source and composition of sputtered ions.	Pick-up ions, e.g. from comets.

***Spitzer's* View on Resolved Debris Disks – Vega, Fomalhaut and β Pictoris**

K. Y. L. Su[1], G. H. Rieke[1], J. A. Stansberry[1], K. R. Stapelfeldt[2], M. W. Werner[2], D. E. Trilling[1], D. C. Hines[3] , M. Marengo[4], S. T. Megeath[4], G. G. Fazio[4], J. Van Cleve[5], [1]Steward Observatory, University of Arizona (933 N Cherry Ave, Tucson, AZ 85721, ksu@as.arizona.edu), [2]JPL/Caltech (4800 Oak Grove Dr, Pasadena, CA), [3]Space Science Institute (4750 Walnut St., Suite 205, Boulder, CO), [4]Harvard-Smithsonian Center for Astrophysics (60 Garden St., Cambridge, MA), [5]Ball Aerospace Corporation (1600 Commerce Str, Boulder, CO).

Introduction: One of the highlights of the *IRAS* mission was the discovery of a large infrared excess around normal stars attributed to dust particles collisionally replenished by asteroids and comets. Debris disks are the most visible signposts of other planetary systems, representing evidence of planetary system formation. *Spitzer* brings new levels of sensitivity and spatial resolution to debris studies in the thermal infrared [1]. Early results from *Spitzer* studies of debris disks around A type stars demonstrate that debris disks come in a huge variety, indicating both a large range in initial planetary system structures and also that individual disks may be dominated by debris created in individual events [2]. The characteristics found in A-star debris disks are analogous to our ideas of the early evolution of the solar system [3]. Here we present the first high spatial resolution far-infrared observations of resolved debris disks: Vega, Fomalhaut and β Pictoris, obtained with the Multiband Imaging Photometer for *Spitzer* (MIPS) [4]. We discuss the results as a whole set and try to understand the diversity of the debris phenomenon. These data provide a foundation for understanding other unresolved debris disks.

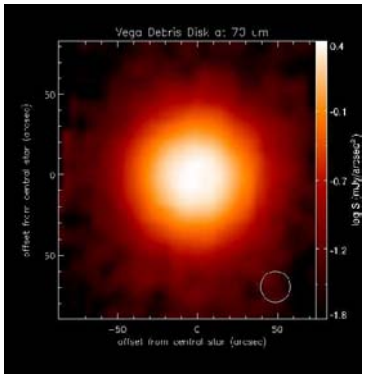

Figure 1 - Vega Disk image at 70 μm. The white circle on the lower left corner indicates the beam size at 70 μm. N is up and E is toward the left.

Vega: The disk around Vega was resolved as face-on disk with a radius of ~22" by *IRAS* [5] and *ISO* [6] at 60 μm. The 850 μm map obtained by Holland et al. [7] with SCUBA on JCMT shows an extended, roughly circular structure with an elongated bright central region oriented NE-SW. Observations at 1.3 mm by Koerner et al. [8] and by Wilner et al. [9] resolved dust emission peaks offset from the star by 8" to 14" that appear to be associated with a ring of emission at a radius of 60 to 95 AU.

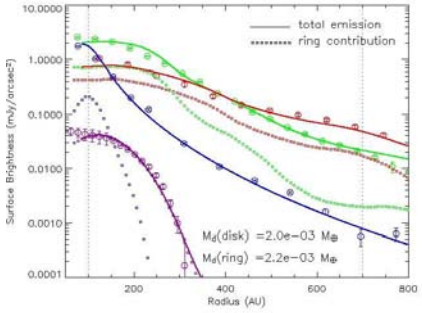

Figure 2 - Radial Surface brightness profiles at 24 (blue), 70 (green) and 160 (red) μm. The open circles are the observed data, and the solid lines are model profiles (see text). SCUBA 850 um is plotted in purple.

Figure 1 shows the disk image (after photosphere subtraction) of Vega at 70 μm. The disk appears very circular, smooth and without clumpiness. The disk angular size is much larger than found previously (at least, ~100" in radius) [10]. Assuming an amalgam of amorphous silicate and carbonaceous grains, the disk can be modeled as an axially symmetric and geometrically think disk, viewed face-on, with the surface particle number density following an inverse radial power law. The disk radiometric properties at 24, 70 and 160 μm are consistent with a range of models using grains of sizes ~1 to ~50 μm. A handful of grain models are consistent with the observed radial surface brightness distributions, but all these models require an 1/*r* surface number density law and a total mass of ~3×10^{-3} earth mass in grains to explain the MIPS observations. A ring, containing grains larger than 180 μm and at radii of 86-200 AU from the star, can reproduce the observed 850 μm flux. The best model fit radial surface profile is shown in Figure 2. This ring could be associated with a population of larger astreroidal bodies analogous to our own Kuiper Belt. Cascades of collisions starting with encounters among these large bodies in the ring produce the small debris that is

blown outward by radiation pressure to much larger distances where we detect its thermal emission. The relatively short lifetime (<1000 years) of these small grains and the observed total mass, set a lower limit on the dust production rate, ~10^{15} g/s. This rate would require a very massive asteroidal reservoir for the dust to be produced in a steady state throughout Vega's life (~350 Myr). Instead, we suggest that the disk we imaged is the aftermath of a large and relatively recent collisional event, and subsequent collisional cascades.

Fomalhaut: A member of the Caster moving group like Vega, Fomalhaut and Vega have similar age, mass and distance. The disk around Fomalhaut was also first found by *IRAS*, and latter inferred as a donut-like disk with ~18" in radius and inclined ~20° from edge-on [11]. Submillimeter maps obtained by Holland et al. [12] and Marsh et al. [13] revealed a ring brightness asymmetry that has been interpreted as a dense clump between the ring ansae, and which might represent the dust particles dynamically trapped in resonance with a perturbing object [14].

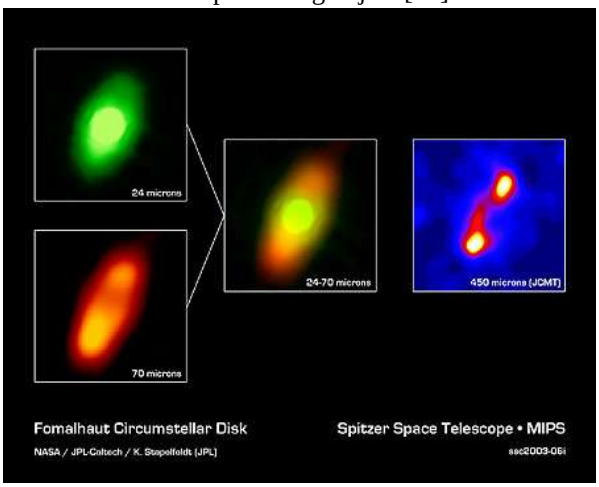

Figure 3 - MIPS images of Fomalhaut debris disk compared to the submillimeter map.

The disk images (after photosphere removal) are shown in Figure 3. While the disk orientation and outer radius are comparable to values measured in the submillimeter (unlike Vega), the disk inner radius cannot be precisely defined: the central hole in the submillimeter ring is at least partially filled with emission from warm dust [15]. The disk surface brightness becomes increasingly asymmetric toward shorter wavelengths, with the S-SE ansa always brighter than the N-NW one. The dusty ansae represent the result of collisional cascades in the asteroidal belt around Fomalhaut seen in submillimeter. The color in the mid-infrared range (20-30 μm) is consistent with an 1/*r* radial density distribution and the inward drift of grains from the outer ring. The new MIPS images suggest that the dust production in Fomalhaut is in a quiescent state, no major dust production event (like the one in Vega) in the past millions years. The dust particles last longer and slow drifting inward under P-R drag before destructed by collisions into smaller particles that are subject to radiation blowout.

β Pictoris: Unlike Vega and Fomalhaut, β Pictoris is a much younger system (~20 Myr) [16]. The amount of dust and gas in this nearly edge-on disk is more abundant than the one in Vega and Fomalhaut. Although the exact gas content in the disk is still in debate. The dust particles in the disk are primarily dominated by small grains that are subject to radiation blowout [17,18,19]. The disk is resolved in *Spitzer* IRS blue (15 μm) and red(22 μm) peakup images as well as MIPS 24, 70 and 160 μm images. Figure 4 shows the disk image at 70 μm with a radius of ~1000 AU. Detail analysis on the resolved multi-color images will be presented in the meeting.

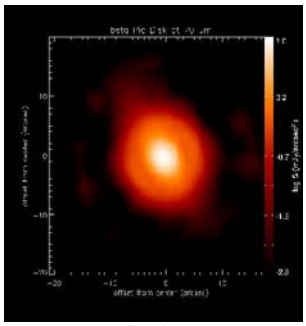

Figure 4 - MIPS 70 μm image of β Pictoris disk.

References: [1] Werner, M. W. et al. 2004, ApJS, 154, 1. [2] Rieke, G. H., et al. 2005 ApJ, 620, 1010. [3] Chambers, J. E. 2004, Earth & Plan. Sci. Letters, 223, 241. [4] Kenyon, S. J., & Bromley, B. D. 2004, ApJL, 602, L133. [5] Aumann, H. H. et al. 1984, ApJL, 278, 23. [6] Heinrichsen, I. Et al. 1998, MNRAS, 293, L78. [7] Holland et al. 1998, Nature, 392, 788. [8] Korener et al. 2001, ApJL, 580, 181. [9] Wilner et al. 2002, ApJL, 569, 115. [10] Su et al. 2005, ApJ, 628, in press. [11] Dent et al. 2000, MNRAS, 314, 702. [12] Holland, W. S. et al. 2003, ApJ, 582, 1141. [13] Marsh, K. A. et al. 2005, ApJL, 620, 47. [14] Wyatt & Dent 2002, MNRAS, 334, 589. [15] Stapelfeldt, K. R. S. et al. 2004, ApJS, 154, 458. [16] Barrado y Navascues, D. et al. 1999, ApJL, 520, 123. [17] Backman, D. & Paresce, F., Protostars & Planets III, p1253. [18] Okamoto, Y. K. et al. 2004, 431, 660. [19] Telesco, C. M. et al. 2005, 433, 133.

CONSTRUCTING THE ZODIACAL CLOUD

M. V. Sykes, Planetary Science Institute (sykes@psi.edu)

Modeling the interplanetary dust cloud has long involved inversion techniques on zodiacal light measurements to determine parametric model components. This contemplates the cloud as something relatively homogeneous, but provided important insights into its distribution and the properties of some of its smallest components scattering visible light. Since the discovery of actual dust production sources by the Infrared Astronomical Satellite, their subsequent observations by other spacebased infrared telescopes, increasingly sensitive and extensive in-situ measurements and sophisticated modeling of the dynamical evolution of dust, the zodiacal cloud can be viewed as the superposition of a number of components of different origins and processes, each of which is subject to focused investigation. These include dust production from the recent collisional disruption of asteroids, the emission of large refractory particles from comets, material arising from collisional processes in the Kuiper Belt and the interloping particles from outside the solar system. This does not necessarily provide a complete picture - there may be evidence of as yet unidentified dust production processes as these components are put back together in an attempt to explain observations of the whole. The study of the modern production of dust in our own solar system provides insight into a variety of evolutionary processes, as well as provides models for the production of dust around other stars.

SIZE DISTRIBUTION OF ANTARCTIC MICROMETEORITES.

S. Taylor[1], G. Matrajt[2], J.H. Lever[1], D.J. Joswiak[2], and D. E. Brownlee[2], [1]Cold Regions Research and Engineering Laboratory, 72 Lyme Rd., Hanover NH 03755, [2] Department of Astronomy, University of Washington, Seattle WA 98195.
Susan.Taylor@erdc.usace.army.mil

Introduction:

Micrometeorites are terrestrially collected extraterrestrial dust particles smaller than about a millimeter. The accretion rate, size distribution and composition of micrometeorites bears on numerous studies including: deducing the compositions of parent bodies; calibrating terrestrial sedimentation rates; interpreting the isotopic record of seawater; linking influx to global climate change; and assessing the role of ET materials in life processes.

In 1995 Taylor et al. [1] retrieved ~ 200g of material from the bottom of the South Pole water well (SPWW) of which about 0.1% were cosmic spherules (melted micrometeorites). Using the particle size distribution, area suctioned and age of ice melted (1100–1500 AD) they computed a terrestrial accretion rate for cosmic spherules 50–700 μm in diameter of 1600 ± 300 tons/yr [1] or 4 ± 2 percent of the flux measured above the atmosphere [2].

We are repeating this analysis using samples collected in 2000 from the SPWW. Compared with 1995 collection, the 2000 samples have less iron-oxide contamination allowing us to find unmelted micrometeorites. We are analyzing the deployment dedicated to the central plateau. Because this area was vacuumed in 1995 the 2000 sample should contain only those particles derived from the older, 700–1100 AD, ice [3] and allow us to calculate a flux for a second time period.

We have found and mounted 3272 micrometeorites from the central plateau sample. We present a preliminary size distribution (as not all micrometeorites have yet been measured) and an estimate of unmelted to melted ratio for the different size fractions.

Methods:

The samples studied were collected in 2000 from the SPWW, a 4,000-m^3 reservoir melting pre-industrial ice. The well's central plateau was vacuumed and yielded ~ 10 g of material. We sieved this sample into >425, 250–425, 150–250, 106–150 and 53–106μm size fractions. Using a binocular microscope we sorted 100% of the >150-μm fractions, 29% of the106-150 fraction and 9% of the 53–106-μm fraction and removed all potential ET grains. We mounted and sectioned over 4000 particles. Using a SEM/EDAX we checked each particle for composition and found that 3272 of particles mounted were micrometeorites. Optical microscopy was used to size the particles and to classify them based on their cross-sectional textures.

Results:

The size distributions for the 1995 and for the 2000 plateau samples are shown in Figure 1. For the 2000 collection we show individual data points for micrometeorites >250μm, as these have all been sized, and plot the cumulative number of micrometeorites for the three smallest size fractions. The numbers of micrometeorites in the smallest two size fractions have been increased to account for the fact that only a portion of each size fraction was sorted. The best-fit line to the tail of the 2000 plateau sample has a slope of -4.5 slightly less steep than the -5.2 tail-slope calculated for the 1995 plateau sample [2]. Nevertheless the two curves are quite similar indicating that the size distributions from the two collections are similar.

The 2000 collection has more micrometeorites than the 1995 collection. The addition of the unmelted component cannot explain the increased number as the unmelted micrometeorites would predominantly change the number of micrometeorites in the smaller size fractions. The fact that we found an order of magnitude more >250μm micrometeorites in the 2000 collection may be due to an increase in the plateau area as the well deepens or to an increase in the flux rate. Although we have not yet measured the plateau area our video records do not show an order of magnitude increase in the plateau area.

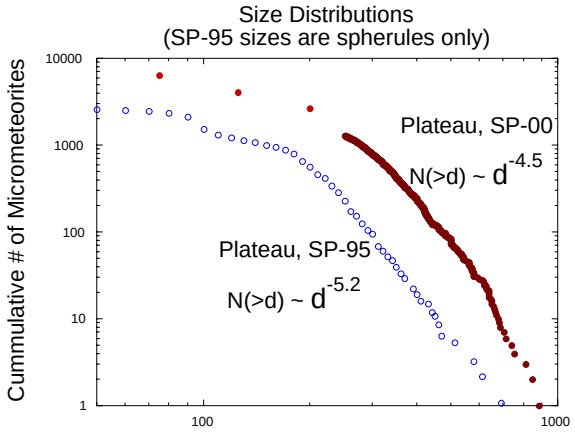

Figure 1. Cumulative size distributions for micrometeorites collected for two different time intervals from the bottom of the South Pole water well.

The numbers of melted and unmelted micrometeorites in each size fraction are given in Table 1. As expected, and noted by others [e.g. 4], the number of unmelted micrometeorites generally increases as the size fraction decreases. We found very few unmelted micrometeorites in the >250μm size fractions and similar number of melted and unmelted micrometeorites in the < 150μm size fractions.

We compare our results with those given for other collections (Table 1). From Greenland ice, Maurette et al. [4] found more un-melted than melted micrometeorites in the <100μm size fraction and about half the number of unmelted as melted in the 100-300μm range. From ice at Cap Prudhomme, Antarctica Maurette et al. [5] found 5 times as many unmelted micrometeorites in the <100μm size fraction and close to half as many unmelted to melted micrometeorites in the 100-400μm size range. Terada et al. [6] sampled ice of three different ages in Antarctica (16, 30 and 60 thousand years before present) and found a range in the unmelted to melted ratio from 0.5 to 4.5 for micrometeorites 40–238μm in diameter. Genge and Grady [7] extracted over 500 micrometeorites from Cap Prudhomme samples and found an

unmelted to melted ratio of ~3. For similarly sized particles, 53–250µm this study, 50–300µm [4] and 40–238µm [6] the unmelted to melted ratios are 0.2, 0.5 and 0.6 respectively. These preliminary results indicate that SPWW collection has a lower number of unmelted micrometeorites than the other two collections. Possible explanations include variations in the types of micrometeorites being deposited, destruction or masking of the unmelted micrometeorites in the SPWW samples and differences in the way micrometeorites are classified. There are many micrometeorites that are transitional between melted and unmelted (Figure 2). How these are tallied can change the unmelted to melted ratio. We intend to photograph all the micrometeorites from the plateau collections and to document how we classified each particle so that the third possibility can be assessed.

Reference	Size fraction (µm)	Number unmelted	Number melted	U/M
This study	>425	1	135	7.41E-03
	250-425	23	1138	2.02E-02
	150-250	134	1288	1.04E-01
	106-150	169	174	9.71E-01
	53-106	70	135	5.19E-01
Maurette et al. 1987	50-100	1500	1060	1.42E+00
	100-200	265	570	4.65E-01
	200-300	45	101	4.46E-01
Maurette et al. 1991	50-100			>5
	100-400			~0.3
Terada et al. 2001	40-238	101	78	1.29E+00
	40-238	134	138	9.71E-01
	40-238	172	84	2.05E+00
	40-238	18	4	4.50E+00
	40-238	30	53	5.66E-01
Genge & Grady 2002	50-400	412	138	2.99E+00

Conclusions:

We expect to calculate a flux for the 700–1100 AD time interval and to complete the particle size distribution for the 2000 SPWW collection this year. Next year we hope to image and classify all the micrometeorites. When complete this collection-level analysis will allow us to place an individual micrometeorite in context and determine how a micrometeorite relates to the population of micrometeorites as a whole.

Acknowledgements: We thank NSF (Dr. Julie Palais program manager) for funding the collection of micrometeorites from the South Pole water well and NASA (Dr. David Lindstrom program manager) for funding the analysis of the 2000 collection. We also thank Sarah (Sally) Elliott for imaging several hundred of these micrometeorites and Dr. Charles Daghlian for use of Dartmouth College's SEM.

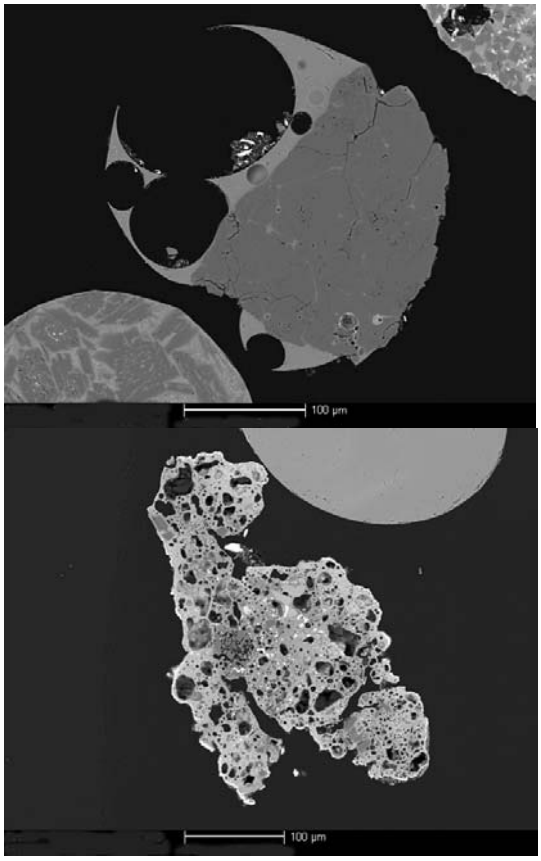

Figure 2. Transitional forms: Relic grain bearing and scoriaceous micrometeorites.

References:

[1] Taylor S, Lever J. H., and Harvey R.P. (1998) Accretion rate of cosmic spherules measured at the South Pole. *Nature* **392**, 899-903. [2] Love S.G. and D.E. Brownlee (1993) A Direct measurement of the terrestrial mass accretion rate of Cosmic dust, *Science* **262**, 550-553. [3] Kuivinen K.C., Koci, B.R., Holdsworth, G.W. and Gow A.J. (1982) South Pole ice core drilling, 1981-1982. Antarctic Journal of the United States XVII, 89-91. [4] Maurette M., Olinger C., Christophe, M., Kurat G., Pourchet, M., Brandstatter, F., and Bourot-Denise, M. (1991) A collection of diverse micrometeorites recovered from 100 tonnes of Antarctic blue ice, *Nature* **351**, 44-47. [5] Maurette M., Hammer C., Brownlee D.E., Reeh N. and Thomsen H.H. (1986) Placers of cosmic dust in the blue ice lakes of Greenland, *Science*, **233**, 869-872. [6] Terada K and 23 others (2001) General characterization of Antarctic micrometeorites collected by the 39th Japanese Research Expedition: Consortium studied of JARE AMMs (III), *Anatarct. Meteorite Res*. **14**, 89-107. [7] Genge M.J. and M.M. Grady (2002) The Distribution of Asteroids: Evidence from Antarctic Micrometeorites, LPSC XXXIII, 1010.pdf.

FE-NI-OXIDE SPHERULES WITH NI-FE-RICH AND FE-AL-RICH SILICATE CORES AND A CHONDRITIC AGGRIGATE SPHERULE FROM DEEP-SEA SEDIMENTS. Y. Tazawa[1] and T. Fukuoka[2], [1]Department of Physics, Graduate School of Science, Kyoto University, Kyoto 606-8502, Japan (tazawa@cr.scphys.kyoto-u.ac.jp), [2]Department of Environmental Systems, Faculty of Geo-Environmental Science, Rissho University, Kumagaya 360-0194, Japan.

Introduction: Deep sea floor is an environment with extremely low rates of sedimentation of terrigeneous particles (*e.g.*, apploxately several mm/10^3 yr for the Pacific Ocean red clay), where is chemically inactive compared to the ground in some cases. Therefore, microparticles of extraterrestrial origin fallen on the Earth extended over 10^4~10^5 years has been preserved in less than a meter-thick of the red clay, though it had been more or less affected by Atmospheric frictional heating, leaching by sea water, biological activity of benthos, *etc.* Spherical microparticles in deep-sea floor (Deep-Sea Spherules, DSSs) which have composition similar to chondrite and/or rich in siderophile elements (SPEs: *e.g.*, Ni, Ir, Os, Au, *etc*.) are thought to be of "cosmic" origin because the shapes seem to be ablation droplets formed during the Atmospheric entry of meteoroids [*e.g.*, 1] in addition to the composition above. They are classified into three groups, typical of them are: (a) iron (metallic, magnetic) spherules (ISs) consist of nickeliferous magnetite and wüstite with or without Fe-Ni metallic cores, (b) stony (silicate) ones (SSs) consist of olivine, magnetite, and glass with chemical composition similar to chondrite, and (c) glassy ones (GSs) consist of glass with the chondritic composition [*e.g.*, 2]. Thermal history and alteration scenario of the spherule formation have been also discussed based on the chemical and mineralogical simulation and observation of internal features [e.g, 3, 4, 5]. DSSs are the important samples thought to be microscopic analogues of meteoroidal and cometary bodies, even though nowadays mass collection of fresh, primitive, and unaltered cosmic particles have been obtained from the Stratosphere and Polar region.

Samples and Experimental: Six DSSs are investigated, which were extracted by sieves and an electromagnet from water-diluted sediments dredged from the 4700 m deep floor at the Central Pacific Ocean (9°30'N, 174°18'W ~ 9°31'N, 174°17'W) by the R/V Hakurei-maru II, Metal Mining Agency of Japan in 1979 and provided for studies on the extraterrestrial matter. Each of them was observed and weighed by using a stereo-zoom microscope and an electro microbalance prior to the analyses.

INAA: They were investigated firstly by instrumental neutron activation analysis (INAA). The procedures were applied basically after [6] and as follows: Four kinds of standards and references were used: (1) glass chips made from JB-1 (GSJ standard rock, basalt, [7]) for the lithophile elements (LPEs), (2) synthetic Ni-platinoid alloy for SPEs [6], (3) ultra-pure synthetic qualtz for references of ^{28}Si (n,p)^{28}Al reaction, and (4) Canyon Diablo iron meteorite (C.D., [8]) for references of SPEs, respectively.

INAA for short-lived nuclides were firstly carried out. The samples were activated individually in sequence with thermal neutron for 5 min at ~2x10^{13} neutrons/cm^2/sec in the pneumatic pipe PN-3 of the reactor JRR-3, the Japan Atomic Energy Research Institute (JAERI), and counted for 400 sec after 2 ~10 min cooling using a gamma-ray counting facility at JRR-3. They were secondly counted for 1000 sec at 1 ~ 6 hr after the first counts at the Inter-University Laboratory for the Joint Use of JAERI Facilities, Research Center for Nuclear Science and Technology (RCNST), University of Tokyo.

INAA for long-lived nuclides were done after those the above. The samples were irradiated together again with thermal neutron for 98 hours at 1x10^{14} neutrons/cm^2/sec in a hydraulic rabbit irradiation facility HR-1 of JRR-3. They were also counted repeatedly in accordance with their half-lives and activities using gamma-ray counting facilities of Aoyama Gakuin University and Gakushuin University.

EPMA: After the INAA study, three ISs and a SS were embedded individually in P-resin. They were sectioned by polishing and coated with carbon to observe textures and distribution of major elements. Each section was photomicrographed with secondary and back scatter electron images (SEI/BEI), and analyzed quantitatively for major and minor chemical composition at several points by a SEM/EDX at Department of Geology and Mineralogy, Kyoto University. Then, it was slightly polished and coated again, and investigated for elemental mapping and point analyses of major elements in the new section by an EPMA at National Institute for Polar Research (NIPR), Tokyo. Both analyzers were operated with an accelerating voltage at 15 KV and probe currents at 14 nA for point analyses and 200 nA for elemental mapping, respectively.

Results and Discussion: Weghts, sizes, and specific gravities (estimated from the weights and sizes) are listed together with the INAA results in Table 1.

Spherules A, B, and C have black shining or metallic luster, and higher specific gravities (4.5 ~ 5.3 g/cm^3), while the D, E, and F have dullish black or dark brown color, or partially translucent blobs, and the lower specific gravities (2.3 ~ 3.1 g/cm^3). These features are usually seen in DSSs. The Spherule D is fragile so that it has partially got out of shape at the time of polishing. CI normalized abundance patterns revealed by INAA and BEIs of the polished sections are shown in Fig 1 and 2.

The B, whose bulk composition assayed by INAA is Fe 67.6%, Ni 4.50%, Co 0.18%, and Ir 2.34ppm, has a mantle of Ni, Co rich Fe oxide, *i.e.*, Fe 69.6%, Ni 4.06%, Co 0.35%, and O 25.3%, and an eccentric spherical core of Ni, Fe rich silicate, *i.e.*, SiO_2 35.2%, NiO 31.8%, FeO 19.1%, Al_2O_3 6.6%, and MnO 3.2%. The C, whose bulk composition is Fe 67.0%, Ni 1.59%, Co 0.24%, and Ir 0.41ppm, has also a mantle of Ni, Co rich Fe oxide, *i.e.*, Fe 71.1%, Ni 1.46%, Co 0.40%, and O 25.6%, and an "amoeboidal (or a walnut-shape)" silicate (glassy?) core consists of Si, Fe, Al, Mg, and K, *i.e.*, SiO_2 64.9%, FeO 17.4%, Al_2O_3 10.9%, MgO 3.68%, and K_2O 2.14%. These kinds of silicate cores have never been observed in IS. One of SS, the D, is a fragile porous aggregate of μ-sized grains of mafic silicates, oxides, and sulphides, whose bulk composition is, *i.e.*, Mg 20.3%, Fe 20.1%, Ni 1.27%, Al 0.46%, Cr 0.20%, Mn 0.10%, Co 484ppm, V 89ppm, Sc 4.91ppm, Os 1.9ppm, Ir 0.51ppm, and Au 0.42ppm, quite similar to CI, except for high Os, Au, and Mg (approx. 4, 3, and 2 times of CI, respectively), and low Al and Mn (approx. a half of CI) contents. Two other SS also have a composition similar to the above SS except for the depletion of SPE.

Acknowledgment: We thank late Prof. K. Yamakoshi, and also K. Nogami for providing the DSSs studied in this work. We thank Y. Ito, H. Sawahata and M. Kawate, RCSNT, University of Tokyo, H. Nagasawa, Gakushuin University, Y. Yokota, Aoyama Gakuin University, M. Kitamura and N. Shimobayashi, Kyoto University, and H. Kojima and N. Imae, NIPR, for making analyzing installations available to us. This work was supported partly by the Inter-University's Program for the Joint Use of JAERI Facilities.

References:[1] Blanchard M. B. et al. (1980) *EPSL, 46,* 178-190. [2] Brownlee D. E. (1985) *Ann. Rev. Earth Planet. Sci., 13,* 147-173. [3] Brownlee D. E. et al. (1984) *Nature, 309,* 693-695. [4] Love S. G. and Brownlee. D. E. (1991) *Icarus, 89,* 26-43. [5] Yada T. et al. (1996) *Proc. NIPR Symp. Antarctic Met., 9,* 218-236. [6] Fukuoka T. and Tazawa Y. (1996) *Abst. 1996 Fall Meeting Jap. Soc. Planet. Sci.*, pp-16. [7] Nagasawa H. et al. (1979) *GCA, 43,* 267-272. [8] Nogami K. et al. (1980) *Geochem. J., 14,* 11-18. [9] Anders E. and Grevesse N. (1989) *GCA,53,* 197-214. [10] Ando A. and Terashima S. (1985) *Abst. Ann. Meeting Geochim. Soc. Jap.* [11] Vdobykin G. P. (1973) *Space Sci. Rev., 14,* 758.

Table 1. INAA Results of Deep Sea Spherules

Sample		A	B	C	D	E	F
Wt[1]	μg	152.1	18.9	12.1	8.9	90.7	17.1
D[2]	μm	400	190	163	195	410	220
SG[3]	g/cm^3	4.5	5.3	5.3	2.3	2.5	3.1
Element							
Al	%	0.253	0.034	0.29	0.46	0.705	0.64
Fe	%	66.0	67.6	67.0	20.1	9.84	25.0
Mg	%	-	-	-	20.3	22.9	23.5
Mn	%	-	0.15	-	0.10	0.326	0.18
Cr	%	0.122	0.202	0.0052	0.202	0.180	0.197
V	ppm	55	96	15	89	77	96
Sc	ppm	1.98	-	1.77	4.91	6.61	6.15
Co	ppm	1810	1820	2360	484	27.5	257
Ni	%	5.16	4.5	1.59	1.27	0.05	0.38
Os	ppm	1.1	-	-	1.9	0.30	-
Ir	ppm	3.97	2.34	0.41	0.51	0.017	0.032
Au	ppm	-	-	-	0.42	0.010	-

Sample		JB-1	Alloy	C.D.	Error(%)	CI	[C.D.]
Wt[1]	μg	31.5	39.8	158.6			
Element							
Al	%	**8.07**	4.11	-	1 - 12	0.868	
Fe	%	**6.3**	-	90.3	1 - 1.5	19.04	92.3
Mg	%	**4.67**	-	-	3 - 13	9.89	
Mn	%	**0.116**	-	-	2 - 10	0.199	
Cr	%	**0.0414**	-	-	1 - 9	0.266	
V	ppm	**207**	-	-	3 - 50	56.5	
Sc	ppm	**28.9**	-	-	1 - 5	5.82	
Co	ppm	**39.1**	23.8	3990	2 - 13	502	4900
Ni	%	-	**82.6**	11.2	3 - 40	1.10	7.25
Os	ppm	-	**52000**	4.7	10 - 50	0.486	3.6
Ir	ppm	-	**1920**	3.62	1 - 28	0.481	2.10
Au	ppm	-	**7410**	2.43	2 - 20	0.14	1.26

Note: 1) Weight in μ g. 2) Diameter. 3) Spacific Gravity. Values bold-faced and underlined are the standard values for the determination, JB-1[10] Alloy [6]. C.D.: Canyon Diablo Iron Meteorite (this work). Error (%): Range of % errors of determination. CI [9]. [C.D.] [11].

Figure 1. CI normalized Abundances of Deep Sea Spherules

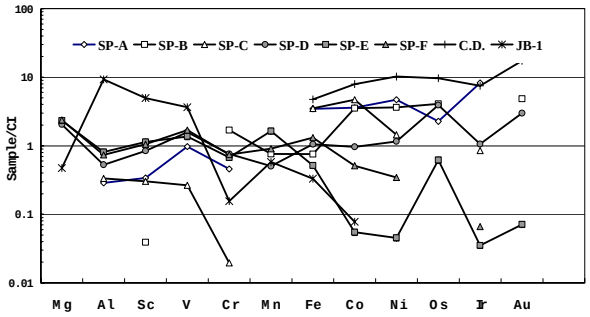

Figure 2. BEIs of Fe-Ni-oxide Spheres with Silicate Cores

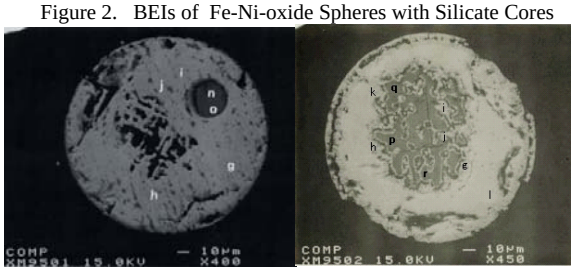

Spherule B Spherule C

INAA RESULTS OF INDIVIDUAL ANTARCTIC MICROMETEORITES AND THEIR TYPES. Y. Tazawa[1], T. Fukuoka[2], Y. Fukushi[2,7], Y. Saito[3], H. Sakurai[4], Y. Suzuki[4], T. Noguchi[5] and T. Yada[6], [1]Department of Physics, Graduate School of Science, Kyoto University, Kyoto 606-8502, Japan (tazawa@cr.scphys.kyoto-u.ac.jp), [2]Department of Environmental Systems, Faculty of Geo-Environmental Science, Rissho University, Kumagaya 360-0914, Japan, [3]Radio Isotope Laboratory, College of Science and Engineering, Aoyama Gakuin University, Sagamihara 229-8551, Japan, [4]Department of Physics, Faculty of Science, Yamagata University, Yamagata 990-8560, Japan, [5]Department of Materials and Biological Science, Ibaraki University, Mito 310-8512, Japan, [6]Department of Earth and Planetary Science, University of Tokyo, Tokyo 113-0033, Japan, [7](Present Address) Department of Earth and Planetary Sciences, Tokyo Institute of Technology, Tokyo 152-8551, Japan.

Introduction: Micro particles thought to be of cosmic origin and collected from the Earth's environments have survived from the heating and the weathering during their Atmospheric entry and their residence on the Earth. Most of them have lost their inherent features and have altered into fully molten droplets, *e.g*., "Cosmic Spherules (CSs)"[1]. Since three decades, a large number of scarcely altered extraterrestrial particles have been collected from the Stratosphere [2, 3] and the Polar Regions [4, 5]. Typical of them are fragile aggregates of chondritic constituents; *i.e*., "Interplanetary Dust Particles (IDPs)" thought to be of cometary origin [2] and "Antarctic Micrometeorites (AMMs), especially, unmelted ones (UMMs)"[4]. AMMs have been collected and investigated widely in recent years [6,7,8,9,10] because it may be found among them that unique samples of primitive Solar System materials have never been known in neither IDPs nor tiny constituents of conventional meteorites.

We report here characteristics of individual AMMs so far investigated by Instrumental Neutron Activation Analyses (INAA)[11,12,13] and their types classified by abundance patterns of LPEs, SPEs and REEs.

Samples: AMMs studied are thirty-one MMs provided by National Institute for Polar Research (NIPR), Tokyo, which were collected from deposits in a storage tank of melting snow for daily life at Dome Fuji Station (DF: 77°19'S, 39°42'E, JARE-37/38)[6], melting and microfiltering bare ice near the Kuwagata Nunatak (KN: 72°06'S, 35°15'E) and south of Minami-Yamato Nunataks (MY: 72°26'S, 35°20'E) at Yamato Mountains (JARE-39)[8], and also melting and microfiltering bare ice near Tottuki Point on the Soya Coast (TP: 68°55'S, 39°51'E, JARE-41)[9]. They are an I-type spherule, fourteen S-type spheres or spheroids, and sixteen S-type UMMs (irregular shape). Three other MMs were also provided but lost during sample preparations for long term neutron irradiations. Assortments and preliminary investigations of the AMMs have been also performed by the AMM initial examination team organized by NIPR [6].

INAA: INAA were performed on the individual MMs and tiny (< 1mm in size) chips of standard materials; *i.e*., glass made from Japanese Standard Rock (basalt) JB-1 (GSJ) for lithophile elements (LPEs), and metal wire Al-Au (0.1%: IRMM-530) and Pt (SRM-680a) for siderophile elements (SPEs). Each of the samples was weighed by an electro-microbalance prior to INAA. We could not use plural gamma-ray counting systems at the same time, so that total numbers of the samples which should be analyzed in a series of INAA including standards and references were to be no more than fifteen or so. Therefore, the MMs were divided into four groups, and four sets of INAA were carried out: *i.e.*, two times of neutron irradiations and consecutive gamma-ray countings should be done in each set. The procedures were applied after [14] and seen in [11,12,13], and as follows:

INAA for short-lived nuclides (SL series). Each of the MMs and the standards was heat-sealed in each small (ca. 2x2 mm^2) bag made with ultra pure polyethylene sheet and irradiated by thermal neutron for 10 min at 20 MW ($1.5x10^{13}$ neutrons/cm^2/sec) in the pneumatic pipe (PN-3) of the reactor JRR-3M, Japan Atomic Energy Research Institute (JAERI). The first counts were done for 400 sec, after 2 ~10 min cooling using a gamma-ray counting facility at PN-3. The second counts were also done for 1000 sec, 1 ~ 6 hr after the end of irradiation, using a facility at the Inter-University Laboratory for the Joint Use of JAERI Facilities, Research Center for Nuclear Science and Technology (RCNST, Tokai br.), University of Tokyo.

INAA for long-lived nuclides (LL series). After the SL series, the samples were picked out from the polyethylene bags and encased again individually in ultra-pure synthetic quartz vials. Then they were activated again all together for 100 hr at 20 MW ($1x10^{14}$ neutrons/cm^2/sec) in the hydraulic rabbit irradiation facility HR-1 of the JRR-3M. They were counted repeatedly in accordance with their half-lives and activities, using gamma-ray counting facilities of Institute for Cosmic-Ray Research, University of Tokyo, and Aoyama Gakuin University. Counting durations and cooling times were about for 2~12 hr after 4~8 days, for 6~24 hr after 2~3 weeks, 1day ~1 week after more than 1 month, respectively.

Results: As shown partly in Table and Figures, results are as follows; *i.e.*, (a) Abundance patterns of LPEs (Al, Ti, Ca, Mg, Cr, Mn, and Na) normalized to CI and Mg, and those of SPEs (Ir, Cr, Mn, Fe, Co, Au) normalized to CI and Fe of the MMs illustrate their features similar to chondrites (except Na, Ir, Au are more or less depleted in two thirds of them) rather than achondrites. (b) As for the LPEs abundances mormalized to CI and Mg (except for those of the I-type MYIB007), Na show the range from $2.2x10^{-3}$ to 1.6, while Al show that from $2.6x10^{-2}$ to 12. The ratios Al/Na also range from $5.5x10^{-1}$ to $3.8x10^{2}$. (c) In contrast to Deep Sea Spherules (DSSs), AMMs do not so much deplete volatile elements; *e.g.*, Na and Au, but fully deplete K. Enrichment of refractory elements do not also show so much (< 11). (d) REE (La, Sm, Yb, Lu) abundances also show those of unfractionated similar to chondrite (eleven MMs), a little fractionated (seven MMs), fractionated (six MMs), and fairly fractionated or not detected (seven MMs). (e) SPEs (Ir,Cr, Mn, Fe, Co, Au) abundances normalized to CI and Fe show those unfractionated (four MMs), unfractionate but with only Ir severely depleted (0.004~0.03 times of Fe, ten MMs), those with Ir and Au depleted (six MMs), those with additionaly rich in Mn (3~6 times of Fe, six MMs) and others (four S-type and an I-type). (f) AMMs studied are classified into six types (five S-types and an I-type) based on the abundance patterns mentioned above.

Acknowledgements: This study was supported partly by the Inter-University's Program for the Joint Use of JAERI Facilities, RCNST, University of Tokyo, the Cooperative Research Program of Institute for Cosmic Ray research (ICRR), University of Tokyo, and also the Cooperative Research Program of NIPR.

References:[1] Murry J. and Reneard A. F. (1883) *Proc. Roy. Soc. Edinburgh, 12,* 474–495. [2] Brownlee D. E. et al. (1976) *NASA Tech. Mem., TMX-73152,* 1-42. [3] CDPET (1981-1997) *Cosmic Dust Catalog, NASA/JSC, Vol. 1-15.* [4] Maurette M. et al. (1986) *Science, 233,* 869–872. [5] Maurette M. et al. (1991) *Nature, 351,* 44–47. [6] Nakamura T. et al. (1999) *AMR, 12,* 183–198. [7] Fukuoka T. et al. (1999) *Ant. Met. XXIV,* 24-25. [8] Yada T. and Kojima H. (2000) *AMR, 13,* 9-18. [9] Iwata N. and Imae N. (2002) *AMR, 15,* 25-37. [10] Noguchi T. et al. (2000) *AMR, 13,* 270-284. [11] Fukuoka T. et al. (2000) *Ant. Met. XXV,* 10-11. [12] Tazawa Y. et al. (2003) *Internatl. Symp. Evolution of Solar System Materials, NIPR,* 138-139. [13] Fukushi Y. et al. (2004) *Ant. Met. XXVIII,* 12-13. [14] Fukuoka T. and Tazawa Y. (1996) *Ant. Met. XXI,* 33-34.

Partial INAA results of AMMs

Sample	F96CB003	F96CB004	F96CB019	F97AG008	MYIB004	MYIB005	MYIB007
wt µg	3.1	3.0	10.7	1.9	3.3	5.8	9.4
Na %	0.07	0.32	0.017	0.77	0.42	0.005	0.002
Mg %	9.5	7.63	20.6	15.0	11.2	11.5	-
Al %	9.84	1.2	0.87	1.52	1.64	1.64	0.037
Ca %	4.08	0.46	0.68	1.70	1.01	2.30	-
Ti %	0.38	-	0.54	-	0.20	0.26	-
Sc ppm	25.8	7.12	5.28	15.1	7.78	8.64	0.17
V ppm	60	48	46	86	68	80	2.4
Cr ppm	3800	2140	149	4370	4980	3800	2800
Mn %	0.12	0.19	0.72	0.28	0.43	0.20	0.01
Fe %	11.3	22.4	11.7	26.2	26.4	27.4	8.86
Co ppm	138	620	57.0	531	435	255	150
La ppm	2.5	0.39	0.21	-	0.25	0.22	-
Sm ppm	-	0.08	0.143	0.320	0.20	0.20	-
Yb ppm	-	0.35	0.31	0.15	0.26	0.32	-
Lu ppm	0.42	0.12	0.09	0.048	0.07	0.03	-
Au ppb	-	3.33	2.64	8.0	2.02	1.5	3.3
Ir ppb	295	775	107	3.79	640	308	34
Type	IVb	I	IVa	IIa	I	IIIb	VI(Iron)
LPEs	L2a	L1b	L4b	L1b	L1a	L3b	L5
REEs	R4a	R3a	R2b	R1b	R2a	R1a	R5
SPEs	S1	S1	S5	S2a	S1	S3	S6

Sample	K5100030	K5100031	K5100033	K5100041	TPND7	TPNJ5	TPNR6
wt µg	3.8	6.8	4.8	1.2	20.5	4.7	13.3
Na %	0.42	0.45	1.22	0.77	0.03	0.03	-
Mg %	15.3	7.6	15.4	11.2	18.5	15.0	30.6
Al %	0.92	1.96	1.16	2.04	1.34	1.75	0.415
Ca %	0.49	0.78	0.97	-	1.41	-	0.458
Ti %	0.27	0.23	-	-	0.10	-	-
Sc ppm	14.0	31.8	8.64	16.4	11.2	11.6	13.9
V ppm	126	62.1	72.4	118	93.1	115	164
Cr ppm	6480	3710	3410	4060	3540	3900	726
Mn %	0.36	0.20	0.36	0.11	0.510	0.217	0.134
Fe %	10.9	26.8	16.9	42.4	13.00	19.60	3.13
Co ppm	15.3	162	107	336	245	127	40.9
La ppm	-	0.59	0.33	2.2	0.28	0.62	0.13
Sm ppm	-	0.689	0.156	0.386	0.199	0.332	0.065
Yb ppm	-	0.38	0.13	0.29	0.256	0.269	0.154
Lu ppm	0.032	0.113	0.030	0.063	0.038	0.052	0.036
Au ppb	-	1.10	4.9	1.80	1.98	2.2	-
Ir ppb	21.7	15.5	1.73	6.87	7.04	13.6	2.73
Type	V	IIb	IIa	IIb	IIIa	IIIb	IVa
LPEs	L2a	L2a	L1b	L2b	L3a	L3a	L4b
REEs	R4b	R2b	R1a	R3b	R1a	R2a	R3a
SPEs	S4	S2a	S2b	S2b	S4	S3	S4

Abundances normalized to CI, Mg (LPS) and Fe (SPE)

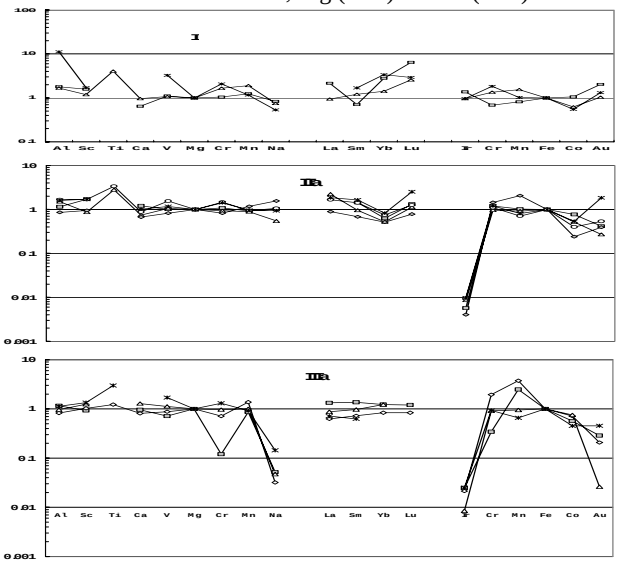

EXPERIMENTAL CONDENSATION OF SILICATE GASES: APPLICATION TO THE FORMATION OF DUST IN CIRCUMSTELLAR ENVIRONMENTS. A. Toppani[1,2*], F. Robert[2], G. Libourel[1,3], P. de Donato[4], O. Barrès[4], L. d'Hendecourt[5], J. Ghanbaja[6], [1]Centre de Recherches Pétrographiques et Géochimiques, Nancy, France, [2]Muséum National d'Histoire Naturelle, Paris, France, [3]Ecole Nationale Supérieure de Géologie, Nancy, [4]Laboratoire Environnement et Minéralurgie (LEM), Nancy, [5]Institut d'Astrophysique Spatiale (IAS), Orsay, France, [6]Université Henri Poincaré (UHP), Nancy, *current address: IGPP, Lawrence Livermore National Laboratory, Livermore, USA, toppani2@llnl.gov.

Introduction: Condensation processes play a major role in the cycle of dust in the galaxy from the formation of interstellar dust to that of the building blocks of our planetary system. However, they are mostly understood via models predicting the chemical composition of the grains condensed at equilibrium in nebular or stellar conditions (e.g. [1]). In order to better understand condensation processes and to evaluate the role of kinetics on the nature of the condensed matter, a new apparatus was developed to perform condensation experiments of multi-elemental refractory gases at various temperatures (25 to 1350°C) and under different pressures (10^{-6} to 1 bar). Here, we present results of condensation experiments performed under thermal non-equilibrium and equilibrium conditions that show the large range of products that can be formed by condensation.

Experimental: Our design [2] consists of a reaction chamber linked to a high-vacuum metal line in which different mixtures of gases can flow. In the reaction chamber, the multi-elemental refractory gas to be condensed is produced by laser ablation (Nd-Yag laser) of a glass target of known composition. We previously showed [2] that the produced gas is not fractionated relative to the target. The ablated glasses were close to "solar" composition [3] for calcium, aluminum, magnesium and silicon (MgO, SiO_2, Al_2O_3, CaO: 36.1, 56.9, 4, 3 wt%), or of Ca-Al rich composition (MgO, SiO_2, Al_2O_3, CaO: 9.3, 48.6, 18.7, 23.4 wt%). Experiments were performed in static mode.

Condensation in non-equilibrium conditions: The non-equilibrium condensation of these refractory gases occurred directly above the target as the hot laser-ablated gas expanding in the cold ambient gas is rapidly supersaturated due to the relatively high pressure in the reaction chamber [4]. This condensation was performed at different total pressures (1 to 30 mbar) of different mixtures of gases (Ar, CO_2, H_2O+CO_2). Temperatures of these ambient gases, i.e. condensation temperatures and durations ranged from 25°C and ~150°C, and from ~40 to 464 min, respectively. The condensed material was collected on a horizontal steel plate 2 to 10 cm above the target. Condensed material collected during these experiments consist of fluffy aggregates of ~10 nm size particles. Their observation by transmission electron microscopy has shown that they are not chemically fractionated (25°C, ±20%) relative to the gas composition and that they are amorphous in almost all explored conditions.

The infrared signatures of the condensed material depend on the nature of the ambient gas. The mid-infrared spectra of products condensed in "dry" CO_2 or Ar gas from Ca-Al-rich or "solar" gas show that only amorphous silicates are present. At the opposite, spectra of material condensed in "wet" CO_2 gas (H_2O + CO_2) show, in addition to the Si-O-Si stretching vibrations feature, three features indicative of the presence of highly bonded water, trapped free water and doubly degenerate asymmetric stretching ν_3 carbonate. The IR characteristics and these features suggest that the carbonate is a complex hydrated carbonate. The far-infrared spectrum of Ca-Al-rich material condensed in "wet" CO_2 shows the bands characteristics of the calcite lattice vibrations [5]. Mid and far infrared spectra of Ca-Al-rich and "solar" condensate indicate thus that the non-equilibrium condensation of the silicate gases in wet CO_2 yields formation of calcium-rich carbonates within a amorphous silicate matrix.

Different tests experiments revealed that carbonates formed directly during the non-equilibrium condensation of the silicate nanoparticles, by a kinetically controlled chemical reaction involving CO_2(g), H_2O(g) and the silicate gas, with P_{H2O} being the limiting parameter. We propose that the reaction proceeds in two steps: (1) hydration in the gas phase of molecular clusters of Ca- or Mg-rich silicate and (2) reaction of these complexes with CO_2(g).

Ca-rich carbonates have been recently detected [5, 6, 7] in planetary nebulae (PN) NGC 6302, NGC 6537 and in several low and intermediate-mass protostars. The main dust component observed in circumstellar envelopes is amorphous silicate [8] thought to have formed by non-equilibrium condensation [8]. Based on our experimental results, we propose that the "astrophysical" carbonates form by chemical reaction between a "hot" silicate gas, and a 300-500K H_2O-CO_2 rich gas during a condensation process far from thermal equilibrium in H_2O(g)-CO_2(g)-rich, high-temperature and high-density regions such as evolved star winds [10] or those

induced by grain sputtering upon shocks in protostellar outflows [11]. Our experiments suggest thus that non-equilibrium vapour phase condensation may be an important mechanism of dust formation in astrophysical environments.

Condensation in equilibrium conditions: In these experiments, a platinum furnace with a positive temperature gradient from bottom to top was located about 2 cm above the target. The fluffy nanoparticles, condensed out of equilibrium above the target, were vaporized at the entrance of the furnace producing a non-fractionnated gas relative the target composition. Because of the temperature gradient inside the furnace, this gas condensed inside the platinum furnace at a controlled temperature (± 20°C). Condensates were deposited directly on a Pt-grid welded to the end of a Pt-Rh10 thermocouple entering the furnace. These Pt-grids were observed by TEM at UHP (Nancy).

The condensation of the "solar" or Ca-Al-rich gas under a total pressure of 10^{-3} bar at temperatures from 1000°C to 1300°C and for run times of 4 to 60 minutes yields direct formation of crystals, oxides or silicates (corundum, spinel, anorthite, melilite, Al-diopside, forsterite and enstatite). The condensed crystals are mainly euhedral to spherical. Crystals show various sizes (50 nm up to 4 µm), with the largest condensed at the highest experimental temperatures and/or the longest run times. They show various textures, from single mineral to aggregates of crystals of similar composition.

The mineralogy of the condensates, close to that predicted at equilibrium, varies with the duration of condensation experiments, with the attainment of a steady state in less than one hour. The mineralogy of the condensates vary also with the temperature of condensation. For instance, the condensation of the solar gas yields the formation of Mg, Si-rich silicates at low-temperature (e.g. enstatite and forsterite at 1045°C) and that of only Al-rich oxides at high-temperature (1280°C). Spinel and corundum occured at all temperatures. The condensation results thus in a chemical fractionation of the gas, i.e. a depletion of the gas in refractory elements at high temperature. However, this study shows also that phases, such as spinel, have favoured kinetics of condensation.

Our experimental results confirm that refractory inclusions in primitive meteorites [12] could have formed by condensation from a hot nebular gas. Similarly, we confirm that crystalline grains can be formed in the outflows of evolved stars by high-temperature condensation. In both cases, our results indicate that kinetic processes certainly influence their mineralogy.

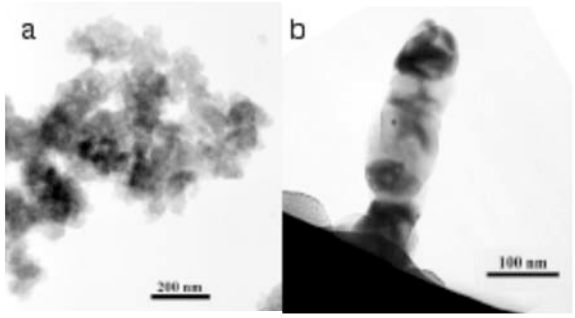

Figure 1: Dust particle formed (a) by non-equilibrium condensation at 25°C in dry CO_2 and (b) by equilibrium condensation at high temperature.

Conclusion: Our experiments show that non-equilibrium low-temperature condensation yields formation of chemically non-fractionated amorphous nanoparticles. In the presence of water vapor, amorphous carbonates can be formed. At the opposite, high-temperature equilibrium condensation does not yield formation of metastable amorphous particles with stochastic composition but of crystalline condensates whose composition is controlled by temperature-time conditions of condensation.

Undifferentiated objects such as comets, asteroids or interplanetary dust. formed, 4,5 Ga year ago, through the aggregation of both interstellar dust formed in the evolved stars and solar dust condensed from the hot nebular gas. Because we successfully reproduced meteoritic or astronomical observations, our experimentally condensed dust particles are valuable analogs of primitive condensates. Our study provide thus information about the physico-chemical environments of formation of these primitive solar system solids.

References: [1] Grossman L. (1969) *Geochim. Cosmochim. Acta, 36*, 597-619. [2] Toppani, A. *et al.* (2004) *Lunar Planet. Sci. Conf.* **XXXV**, #1726. [33] Anders, E., Grevesse, N. (1989) *Geochim. Cosmochim. Acta* **53**, 197-214. [4] Chen, L.-C. (1994) in *Pulsed Laser Deposition of Thin Films*, ed. Chrisey & Hubler, 167-198. [5] Kemper, F. *et al.* (2002) *Nature* **415**, 295-297. [6] Ceccarelli, C. et al. (2002) *Astron. Astrophys.* **395**, L29-L33. [7] Chiavassa, A. et al. (2005) *Astron. Astrophys.* **432**, 547-557. [8] Tielens, A.G.G.M. *et al.* (1998) *Astrophys. Space Sci.* **255**, 415-426. [9] Gail, H.-P. *et al.* (1999) *Astron. Astrophys.* **347**, 594-616. [10] Ferrarotti, A.S. and Gail, H.-P. (2005) *Astron. Astrophys.* **430**, 959-965. [11] Van Dishoeck, E.F. (2004) *Annu..Rev.Astron.Astrophysics* **42**, 119-167 [12] Christophe M.l. (1968) *Bull. Soc. Fr. Minéral. Cristallogr.*, **91** , 212-214.

DUST SAMPLES FROM COMET WILD 2 AND INTERSTELLAR STREAM. P. Tsou[1], D.E. Brownlee[2], F. Hörz[3], G. Flynn[4], L. Keller[3], K. McKeegan[5], S. A. Sandford[6], M. E. Zolensky[3], [1]Jet Propulsion Laboratory, California Institute of Technology, (peter.tsou@jpl.nasa.gov), [2]Astronomy Department, University of Washington, [3]NASA Johnson Space Center, [4]State University New York-Plattsburgh, [5]University of Californa, Los Angeles, [6]NASA Ames Research Center

Introduction: STARDUST is the first mission designed to bring samples back to Earth from a known comet and also the first to bring back contemporary, free interstellar particles[1]. On January 2, 2004, for about five minutes about 19:21:32 UTC, STARDUST captured dust grains from comet 81P/Wild 2 at 236.4 ± 1 km from the nucleus [2]. On the reverse side of the Wild 2 sample collector tray, there are equal number of aerogel capture cells optimized to capture dust from the contemporary interstellar stream in the 2 AU range [3]. Interstellar dust collection began on February 16, 2000 through May 20, 2000 and again from July 27, 2002 through December 9, 2002, a total of 246 days.

Uniqueness of Samples: Wild 2 is a unique comet for coma sample return since it was relatively "fresh". Our sample collection was only the fifth perihelion passage. In 1974, the comet had a close encounter with Jupiter that dramatically changed its orbit [4]. The comet now has a perihelion distance of 1.58 AU and an aphelion near Jupiter's orbit at 5.2 AU. The outer layers of Wild 2 have only been subjected to moderate solar heating allowing our samples to be more representative of the nucleus composition. Wild 2 samples represent well-preserved relics of the outer regions of our solar nebula and fundamental building blocks of our planetary system.

Interstellar grains are the main repositories of condensable elements, which permeate the galaxy. On the average, interstellar grains are expected to be considerably smaller than Wild 2 particles, mostly in the submicron size range, although interstellar particles as large as 10 μm are distinctly possibility [5]. It is most advantageous to capture these particles when the spacecraft's orbit carries it in the same direction as the interstellar dust stream's velocity vector to reduce the capture speed by the amount of the spacecraft speed. For STARDUST, this occurred as the spacecraft was on the inbound portion of the orbit.

The unique opportunity for STARDUST is to study the interstellar grains accreted in Wild 2 at the formation of the comet which can now be compared with dust captured from the contemporary interstellar stream, possibly billions of years apart.

Sample Instrument: These solid samples are captured in two back-to-back sample collection trays occupied by newly developed smooth-gradient-density silica aerogel. There are 132 silica aerogel capture cells of 3 cm and 1 cm thickness for the cometary and the interstellar sides, respectively. The aerogel capture cells were wedged into the sample collection trays and wrapped on all four sides with 101.6 μm thick 1100 aluminum foil to facilitate aerogel capture cell removal as well as serving as a small grain capture medium. The total exposed Wild 2 aerogel surface area is 1039 cm^2 and 153 cm^2 of aluminum foil.

Preliminary Examination: On January 15, 2006, these samples will be returned to Earth in a direct reentry capsule at the Utah Test and Training Range. There are about 150 sample analysts in six disciplines (optical, composition, mineralogy/petrology, isotopes, organics and cratering) who will participate in the Preliminary Examination of the Wild 2 samples. Preliminary results for Wild 2 will be reported by September 2006 and the interstellar samples results a year later.

References:

[1] Brownlee, D. E. et al. (2003) *JGR, 90,* 1151–1154. [2] Tsou P. et al. (2003) *JGR, 32,* A74. [3] Tsou P. (2004) *JGR,*. [4] Sekanena S.. (2003) *JGR*. [5] Grün et al., (1993) *Nature*.

A LARGE AREA COSMIC DUST COLLECTOR ON THE INTERNATIONAL SPACE STATION. P. Tsou[1], F. Giovane[2], R. Corsaro[2], J. C. Liou[3], [1]Jet Propulsion Laboratory, California Institute of Technology (peter.tsou@jpl.nasa.gov), [2]Naval Research Laboratory, [3]ESCG/ERC at NASA Johnson Space Center.

Introduction: The Large Area Dust Collector (LAD-C), ten-square meter (10 m^2) of instrumented silica aerogel mounted externally on the International Space Station (ISS) [1], will capture and return large dust particles intercepted in Earth orbit. The uniqueness of LAD-C is that it carries a self-contained acoustic impact recording and locationing system to offer the opportunity to determine the particles' trajectories nondestructively. With which LAD-C can provide, for the first time, an opportunity to ascertain the particles' parent sources.

Another uniquness of LAD-C is that the flight cost for space deployment, integration and Earth return will be provided by the Department of Defense (DoD) Space Test Program (STP). The cost of the flight instrument itself is furthered shared among science and space debris participants.

Technologies: LAD-C makes use of matured silica aerogel capture medium developed at Jet Propulsion Laboratory (JPL) for Space Shuttle Get Away Special Sample Return Experiment, the Mir Sample Return Experiment and the STARDUST mission, the 4th Discovery Program. The self-contained capture time acoustic recording system, originally concieved and developed at the JPL [1], offers nondestructive particle trajectory determination. The acoustic system was subsequently further developed and demonstrated under a NASA Planetary Instrument Definition and Development (PIDD) Program in a joint effort between JPL, JSC and the US Air Force Academy, led by the Naval Research Laboratory (NRL).

Consortium: A highly leveraged consortium of technologies and resources has been organized for LAD-C: DoD provids the flight through an agreement with NASA, NRL provides experiment management and the acoustic system, NASA Orbital Debris Program Office provides debris and dust dynamics and modeling, the US Naval Academy provides and adjunct uplink/downlink system for real-time examination, and JPL provides the experiment concept and capture medium. Other participants are under discussion, each contributing appropriate resources to accomplish this overall LAD-C experiment.

This LAD-C experiment serves both the cosmic dust science community in capturing rare large (~100 μm) extratresstrial dust particles from asteroids and comets and possible dust from interstellar sources. For the space debris community, LAD-C provides statistics for smaller (< 1mm) sized orbital debris [3]. The International Space Station offers a unique opportunity for a long term space platform from which larger sized particles from large number of sources can be collected. For the dust community, LAD-C revives the desire for the Cosmic Dust Collection Facility that was cancelled as an External Attached Payload on the Space Station Freedom in 1988.

Science Return: LAD-C flight will provide: 1) statistical significant samples of ~thirty 100 μm large extraterrestrial particles for an one year exposure; 2) the potential of assigning the parent sources of the captured particles; 3) the retrieval of samples themselves for detailed Earth based laboratory analysis to determine the chemical and physical nature of the particles; 4) demonstration for a low-cost and long term sampling of a large number of solar system bodies on the space station, a NASA's goal to promote the external usage of the ISS.

References: [1] Corsaro, R. et al., (2004) Orbital Debris Quarterly News. [2] Tsou, P., (1988), LPI TR 88-01. [3] Liou, J.-C. et al., (2005) Proceedings of the 4th European Copnference on Space Debris.

WIZARD – A new observation system of the zodiacal light

Munetaka Ueno[1] (ueno@zodiacal-light.org), Masateru Ishiguro[2], Fumihiko Usui[2], Ryosuke Nakamura[3]
Takafumi Ootsubo[4], Naoya Miura[1], Yuki Sarugaku[2], Suk Minn Kwon[5], SeungSoo Hong[6], Tadashi Mukai[7]
[1] Department of Earth Science and Astronomy, University of Tokyo, 3-8-1 Komaba, Meguro, Tokyo 1538902 Japan
[2] Institute of Space and Astronautical Science, Japan Aerospace Exploration Agency
[3] National Institute of Advanced Industrial Science and Technology, [4] Nagoya University
[5] Kangwon National University, [6] Seoul National University, [7] Kobe University

Introduction: We developed a new observation system WIZARD; "***W**ide-field **I**mager of **Z**odiacal light with **Ar**ray **D**etector*" (Figure 1). Since the zodiacal light is faint and very extended all over the sky, WIZARD employs a sensitive CCD and a wide field optics with sufficient spatial resolution to measure the contribution of integrated flux of the individual stars. WIZARD is designed to measure the absolute brightness of the diffuse sky at visible wavelength and to have good stability of the system zero-level as well as low noise feature. The first light of WIZARD was performed in 2001 at Mauna Kea, Hawaii, and the first scientific image of the gegenschein was taken in 2002 under collaboration with SUBARU observatory. We have been promoting extended observations of the zodiacal light along the ecliptic plane, for three years at NASA/ IRTF's site. We present the design and the performance of WIZARD system, and also the preliminary results of our observations.

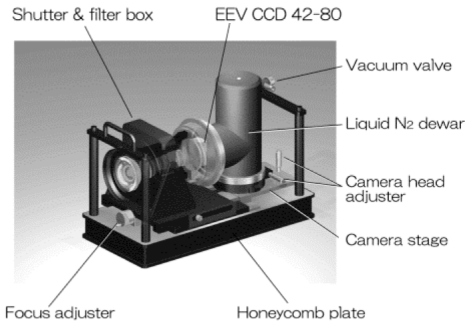

Figure 1 WIZARD system

WIZARD system: The stability of the CCD camera is very important issue to measure the absolute brightness of zodiacal light, because it extends even beyond the wide field of view of WIZARD, which means that it is still hard to assign the zero-level within the image. WIZARD employs a liquid-nitrogen cooled dewar to operate the CCD (EEV CCD 42-80) to minimize the temperature fluctuation of the CCD device, which causes unexpected uncertainty of the zero point of the photometry. The device has large imaging area, 27.6 x 55.3 mm^2 with 2048 x 4096 pixels, and quantum efficiency of 90 % at 460 nm. The optics is also designed very carefully to realize efficient observations, and has F-ratio 2.8 and focal length 32.5 mm (much shorter than the device size!), giving field-of-view of 49 x 98 square degree of arc and the plate scale of 86 arcsec./pixel. The lens system is designed and manufactured by Genesia Corporation in Japan. The band-pass filter is placed at a position of the optical pupil, and also specially developed to suppress the airglow emissions (Figure 2). The CCD, the shutter, and the mounting are controlled by COGITO-3, a multi CCD control system.

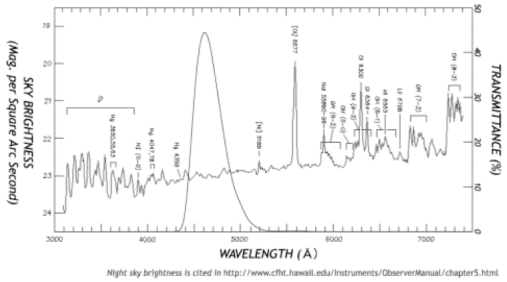

Figure 2, Transmittance of the filter and the airglow

Observations: The zodiacal light images taken by WIZARD are shown in Figure 3.

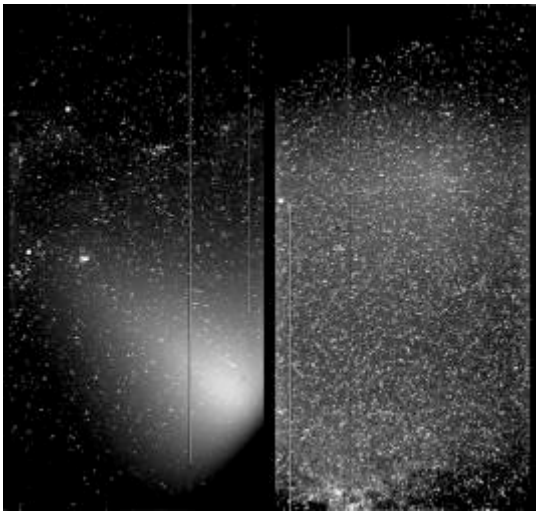

Figure 3. The evening zodiacal light (left) and the gegenschein (right), with the exposure time 180 sec. and 300 sec., respectively.

A DYNAMIC FOUNTAIN MODEL FOR DUST IN THE LUNAR EXOSPHERE.

R. R. Vondrak, T. J. Stubbs and W. M. Farrell, NASA Goddard Space Flight Center, Greenbelt, MD 20771, USA, Timothy.J.Stubbs@gsfc.nasa.gov.

Introduction: During the Apollo era of exploration it was discovered that sunlight was scattered at the terminators giving rise to "horizon glow" and "streamers" above the lunar surface [1,2]. This was observed from the dark side of the Moon during sunset and sunrise by both surface landers and astronauts in orbit (Fig.1). These observations had not been anticipated since the Moon was thought to have a negligible atmosphere or exosphere. Subsequent investigations have shown that the sunlight was most likely scattered by electrostatically charged dust grains originating from the surface [2,3,4,5,6]. This dust population could have serious implications for astronomical observations from the lunar surface [7] and future exploration [8].

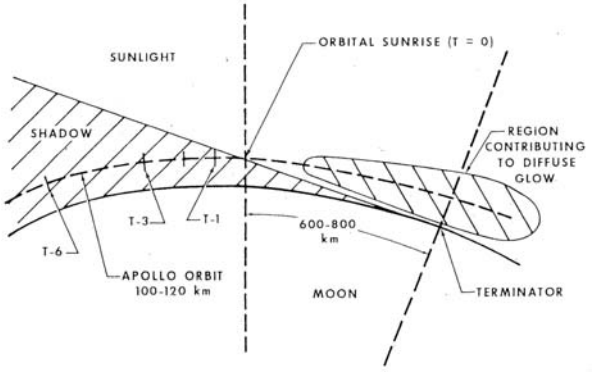

Fig. 1. Schematic showing a cross-section of the Moon in the plane of the Apollo orbit (dashed line). This depicts the physical situation consistent with Apollo 17 observations of "horizon glow" and "streamers" [1].

The lunar surface is electrostatically charged by the local plasma environment and the photoemission of electrons by solar UV and X-rays [8]. Under certain conditions, the like-charged surface and dust grains act to repel each other, such that the dust grains are ejected from the surface [2,3,4].

A dynamic "fountain" model has recently been proposed, as illustrated in Fig. 2b, to explain how submicron dust can reach altitudes of up to ~100km [10,11]. Previous static dust levitation models focused on heavier micron-sized grains near the surface, which did not explain the presence of much lighter grains at higher altitudes. By relaxing the static constraint, [10] showed that grains can be "lofted" to high altitudes under the action of dynamic forces. Here we aim to improve the dynamic fountain model by including more realistic electric field profiles [12] and new results relating to grain cohesion at the surface [13].

Apollo-era Observations: Horizon glow (HG) observed by the Surveyor-7 lander was most likely caused by electrostatically levitated ≈5μm dust grains at heights of ~10cm near the terminator [3]. HG observations were ~10^7 times too bright to be explained by secondary ejecta from micro-meteoroid impacts [2,3].

Astronaut observations of orbital sunrise revealed HG and streamers above the lunar surface (Fig. 1) varying on ~1–100s timescales. This indicated that they were produced by light scattering in the lunar vicinity by particles that were present sporadically [4]. The HG had a scale height of ~10km, so was unlikely to be caused by gases in the lunar exosphere [6].

The Lunar Eject and Meteorites (LEAM) experiment on the Moon detected the transport of electrostatically charged lunar dust [5]. The dust impacts were observed to peak around the terminator regions, thus indicating a relationship with the HG observations.

HG appeared as "excess" brightness in photographs taken from orbit of the solar corona above the lunar terminator. Excess brightness could not be accounted for by a co-orbiting cloud of spacecraft contaminants [1]. This evidence strongly suggested the presence of a variable lunar "atmosphere" of ~0.1μm dust extending to altitudes >100 km created by some electrostatic suspension mechanism [4,5].

Dynamic Dust Fountain Concept and Model: Fig. 2 shows a schematic comparing (a) the static levitation concept [1,2,3] with (b) the evolution of a dust grain in the dynamic fountain model [10]. In the levitation model the dust grain finds a point near the surface where the electrostatic (F_q) and gravitational (F_g) forces acting on it are about equal and opposite, and it is thus suspended. In the dynamic fountain model, once the dust grain has attained sufficient charge to leave the lunar surface (i.e., $F_q > F_g + F_c$), it is accelerated upward through a sheath region with a height ~λ_D (plasma Debye length). (Note: F_c is the force of grain cohesion at the surface.) The dust grains in question are so small that initially $F_q >> F_g$, such that the dust grains leave the sheath region with a large upward velocity (V_{exit}) and follow a near-parabolic trajectory back toward the lunar surface since the main force acting on them now is gravity.

Initial Results: Surface charging in the model is photo-driven on the dayside and plasma electron-driven on the nightside [8]. Fig. 3 shows the maximum height reached by a dust grain (Z_{MAX}) as a function of r_d and the angle from the subsolar point (θ) for typical solar wind conditions [10]. This suggests that dust can

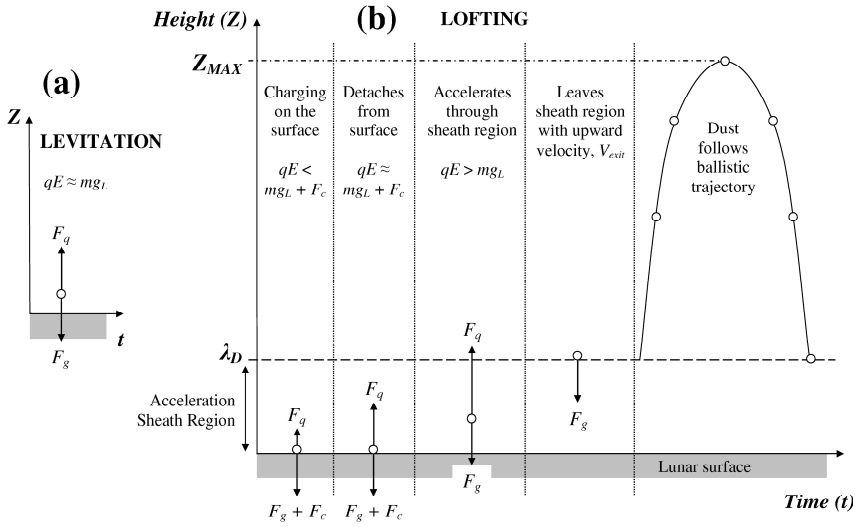

Fig.2. (left) Schematic comparing (a) the static levitation concept with (b) the evolution of a dust grain in our dynamic fountain model [10]. Forces on the grains: electrostatic (F_q), gravitational (F_g), and grain cohesion at the surface (F_c).

Fig. 3. (below) Spectrogram plot showing the maximum dust grain height reached (Z_{MAX}) as a function of angle from the subsolar point (θ) and dust grain radius (r_d) [10].

be lofted at most locations on the lunar surface, apart from in the region just sunward of the terminator labeled the "Dead Zone" ($\theta \approx 80°$), where the electrostatic surface potential $\phi_S \approx 0$. Fig. 3 also shows that at the terminator dust grains <0.1μm can be lofted to ~1–100km.

Discussion: In the model presented by [10] neglected effects included: (1) grain adhesion to the surface [14], (2) secondary electron currents [9,15,16], (3) realistic surface electric field profiles [12] and horizontal electric fields at the terminator [17], (4) the lunar wake electric fields near the terminator [18], (5) collective behavior on dust grain charging [16].

In order to improve the accuracy of this model we will include more realistic surface electric field profiles and grain cohesion at the surface. Inclusion of realistic surface electric field profiles [e.g., 12] is unlikely to affect the Z_{MAX} reached by the lightest grains; however, it will likely significantly increase the time-of-flight estimates. Grain cohesion at the surface is anticipated to limit dust transport for surface potentials <10V [13], although estimates of this effect still require significant refinement.

Conclusions: From a comparison with [7] it appears that sub-micron dust grains could contaminate astronomical observations of infra-red, visible and UV light over a significant portion of the lunar surface, and not just at the terminator. This one of many ways in which dust could interfere with science and exploration activities on the Moon [8], therefore a thorough understanding of lunar dust behavior is necessary in order to effectively tackle future problems.

Acknowledgements: T.J.S. funded by NRC. Thanks to J.S. Halekas for LP/ER data. Fig. 1 courtesy of J.E. McCoy.

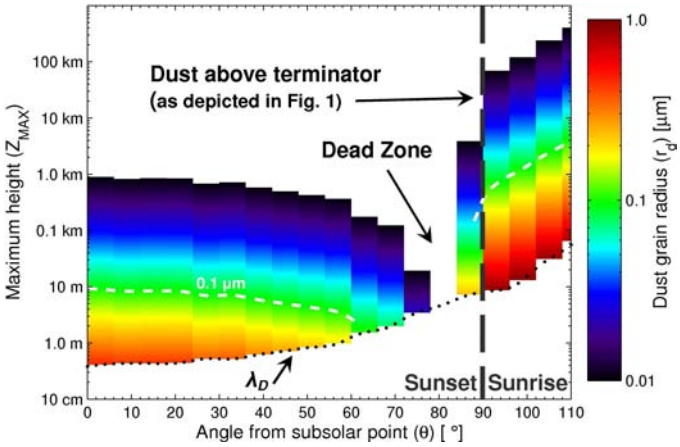

References: [1] McCoy, J.E. (1976) Proc. Lunar Sci. Conf. 7th, 1087. [2] Rennilson, J.J. and Criswell, D.R. (1974) The Moon, 10, 121. [3] Criswell, D.R. (1973) Photon & Particle Interactions with Surfaces in Space, 545. [4] McCoy, J.E. and Criswell, D.R. (1974) Proc. Lunar Sci. Conf. 5th, 2991. [5] Berg, O.E., et al. (1976) Interplanetary Dust and Zodiacal Light, 233. [6] Zook, H.A. and McCoy, J.E. (1991) Geophys. Res. Lett., 18, 2117. [7] Murphy, D.L. and Vondrak, R.R. (1993) Proc. Lunar Planet. Sci. Conf. 24th, 1033. [8] Stubbs, T.J., et al. (2005) Lunar Planet. Sci. Conf. 36th, 2277. [9] Manka, R.H. (1973) Photon & Particle Interactions with Surfaces in Space, 347. [10] Stubbs, T.J., et al. (2005) Adv. Space Res., in press. [11] Stubbs, T.J., et al. (2005) Lunar Planet. Sci. Conf. 36th, 1899. [12] Nitter, T. et al. (1998) J. Geophys. Res., 6605. [13] Starukhina, L.V. (2005) Lunar Planet. Sci. Conf. 36th, 1343. [14] Rhee, J.W. et al. (1977) COSPAR Space Res. 17th, 627. [15] Horányi, M. et al. (1998) Geophys. Res. Lett., 103, 8575. [16] Goertz, C.K. (1989) Rev. Geophys., 27, 271. [17] Berg, O.E. (1978) Earth Planet. Sci. Lett., 39, 377. [18] Farrell, W.M. et al. (1998) Geophys. Res. Lett., 103, 23,653.

CHARACTERISTICS OF DUST PARTICLES OBSERVED BY CASSINI AT SATURN'S RING PLANE CROSSINGS. Z. Z. Wang, D. A. Gurnett, T. F. Averkamp, A. M. Persoon, and W. S. Kurth (University of Iowa, Dept. of Physics and Astronomy, Iowa City, IA 52242,USA; zhenzhen-wang@uiowa.edu).

The Cassini spacecraft passed over the rings of Saturn on July 1, 2004. Figure 1 shows the trajectory of the Cassini spacecraft. The spacecraft passed northbound through the ring plane between the F and G rings on the inbound pass and southbound between the same two rings on the outbound pass. The inbound ring plane crossing occurred at 00:46:31 Universal Time (UT) at a radial distance of 2.634 R_S (R_S = 60,286 km). The outbound ring plane crossing occurred at 04:33:51 UT at a radial distance of 2.630 R_S. At both ring plane crossings very intense impulsive signals were detected by the Radio and Plasma Wave Science (RPWS) instrument on the spacecraft. The noise is attributed to small micron-sized dust particles striking the spacecraft.

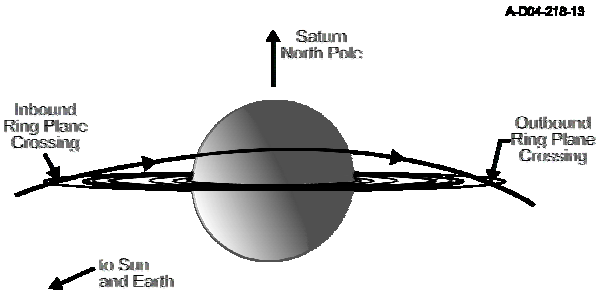

Figure 1. Cassini trajectory at Saturn encounter.

When a small high-velocity dust particle strikes the spacecraft, the kinetic energy is converted into heat which vaporizes both the particle and part of the spacecraft target, thereby producing a small partially ionized plasma cloud. The electrons in the plasma cloud expand from the impact site at high velocities, forming an electric field between the spacecraft body and the escaping plasma cloud. As the electric field sweeps outward, it induces a voltage in the antenna, which is a function of the charge released by the impact. Since laboratory measurements have shown that the charge released is proportional to the mass of the impacting particle [1], these measurements provide information on the mass and size distribution of the dust impacts. The dust impact rate is one of the most basic quantities that can be determined from the RPWS waveform data. Figures 2 and 3 illustrate the impact rate *R* as a function of time (UT) and distance above/below the equatorial plane (*z*) for the inbound and outbound ring plane crossings. In both cases the impact rate reaches a maximum value very close to the equator crossing. Making the assumption that the particle distribution depends only on the distance *z* from the equatorial plane, the impact rate can be fit to a combination of Gaussian curves using the function

$$R = R_0 + R_1 e^{-(z-h)^2/L_1^2} + R_2 e^{-(z-h)^2/L_2^2},$$

where *h* is the offset from the equatorial plane and L is a measure of the thickness of the respective Gaussian component. The fit parameters for the inbound ring plane crossing are listed in Figure 2. In this case the impact rate from the Gaussian fit reaches a maximum value of 1164/second.

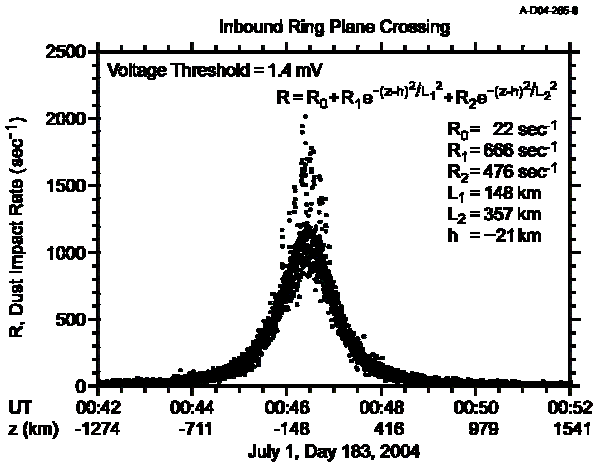

Figure 2. Dust impact rate on inbound ring plane crossing.

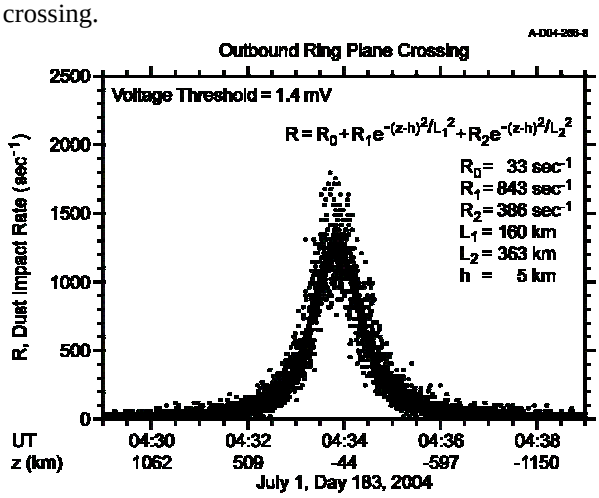

Figure 3. Dust impact rate on outbound ring plane crossing.

Figure 3 illustrates the impact rate and the best Gaussian fit (shown as a solid line) for the outbound ring plane crossing. The impact rate from the Gaussian fit reaches a maximum value of 1262/second, again very close to the equator. The fit parameters for the outbound crossing are listed in Figure 3.

The mass distribution depends on the distance from the ring plane and varies approximately as m^{-2} near the center of the ring plane at $z = 0 \pm 70$ km. The rms mass estimated from the voltage spectrum is about 8×10^{-11} grams, giving a corresponding size of 2.3 μm, on the order of a micron.

Reference:

[1] Grün, E. (1981) *ESA Rep., SP-155*, 81.

THE FUNDAMENTAL ROLE OF PHOTOPHORESIS FOR DUST IN PLANETARY SYSTEMS. G. Wurm[1] and O. Krauss[1], [1]Institute for Planetology, Wilhelm-Klemm-Str. 10, D-48149 Münster, Germany, e-mail: gwurm@uni-muenster.de.

Introduction: It is common knowledge that radiation pressure is important for the dynamics of dust in optical thin environments like the Solar System or debris disks. In very young systems like protoplanetary disks particles are embedded in a gaseous environment, and it is also common knowledge that this gas will drag particles along. However, if dust particles are embedded in a gaseous AND optical thin disk another effect emerges – photophoresis. Though this force is known since at least 1874 [1], it has been treated extremely stepmotherly. It almost completely escaped attention in space science and astrophysics so far, though this force can be extraordinarily strong, e.g. it can be orders of magnitude larger than radiation pressure, as nicely illustrated by "light mills".

Photophoresis in Space: There is little doubt that the conditions necessary for photophoresis to work exist in a more or less transitional stage from dense protoplanetary disks to debris disks. Solids and gas are separate components and evolve quite differently. While the dust aggregates to planetesimals, protoplanets, and planets on timescales of a few million years the gas stays for about ten million years [2][3][4]. With the dust getting depleted the disk turns optically thin. Small particles will quickly move outwards due to photophoresis then. Photophoresis will clear the inner disk of all small bodies and will concentrate particles in rings around a star. With typical parameters assumed (minimum mass Solar Nebula, low thermal conductivity of porous dust aggregates) a concentration will occur at regions of several tens of AU suggesting a link to the Kuiper belt [5]. For other systems like HR 4796A with the given star parameters and assuming a twice as massive gas disk, a concentration would occur at about 60 AU [6]. This is seen in Fig. 1 which shows the ratio of the photophoretic (and radiation pressure) force to residual gravity. The position can be perfectly matched with the inner edge of the observed dust ring [5][6].

While the gas might be dispersed at a certain time, the photophoretic concentration might have triggered the formation of Kuiper belt objects by then and provided the reservoir for the observed dust produced in collisions of larger bodies. In total, dust properties will not only depend on the reservoir that originally existed in the outer region but a significant fraction of solids might be a mixture of dust from the whole inner system transported outwards. Photophoresis is a very effective mechanism to transport solid particles outwards.

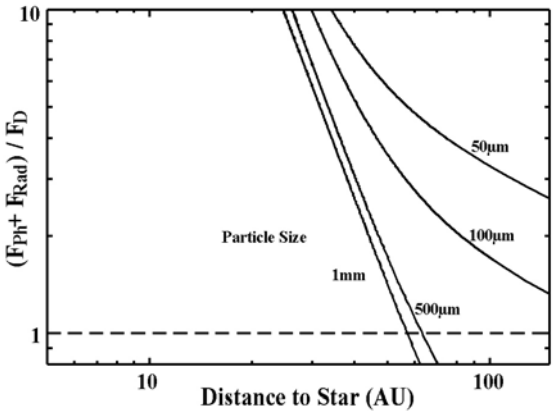

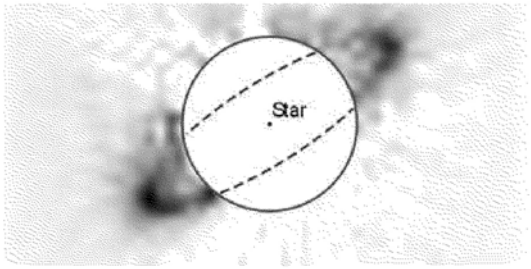

Fig. 1 Photophoretic force (+rad. pres.) to residual gravity. Rings would form at a ratio of 1. Below: HST image (inverted) of HR 4796A matched by this model.

Photophoresis will also concentrate *compact* particles like chondrules found in meteorites closer to the sun. Assuming "typical" parameters photophoresis would concentrate these particles in the asteroid belt region [7].

Certainly, photophoresis plays a limited role for the motion of a dust particle in the current, essentially gas-free Solar System. However, it might have been a major factor for – if not triggering the formation of the two most important dust reservoirs in the Solar System – comets from the Kuiper belt and the asteroids [5][7].

References: [1] Crookes W. (1874) *Proc. Phys. Soc. London, 1,* 35–51. [2] Haisch K. E., Lada E. A., and Lada C. J. (2001) *ApJ, 553,* L153–L156. [3] Greaves J. S. (2004) *MNRAS, 351,* L99–L104. [4] Takeuchi T. et al. (2005) *ApJ, 627,* 286–292. [5] Krauss O. and Wurm G. (2005) *ApJ,* (accepted). [6] Wahhaj Z. et al. (2005) *ApJ, 618,* 385–396 [7] Wurm G. and Krauss O. (2005) *Icarus,* (submitted).

LARGE SAMPLES OF CHONDRITIC INTERPLANETARY DUST PARTICLES IN CHONDRITIC METEORITES.

M.E. Zolensky. KT, NASA Johnson Space Center, Houston, TX 77058, USA (michael.e.zolensky@nasa.gov).

Introduction: We know that the parent asteroids of the bulk of the chondritic interplanetary dust particles (IDPs) are not represented by known meteorites [1-4]. However, we should expect to find samples of these materials within existing regolith breccias, and over the past several years we have identified two likely candidates.

Ningqiang Chondrite: Ningqiang is a unique carbonaceous chondrite, though with some similarities to the oxidized CV3s. We have published a report on a large (5mm) Ningqiang dark inclusion [5]. This Ningqiang dark inclusion appears to record the following processes: (1) formation (condensation and Fe-enrichment) of olivine crystals in the nebula with compositions of Fo_{42-62}, (2) irradiation resulting in amorphitization of the olivine to varying degrees, and pyrrhotite formation, (3) partial annealing resulting in fairly large, euhedral, olivine and pyroxene grains with remnant amorphous sharply-bounded rims, (4) in some cases prolonged annealing resulting in microcrystalline olivine or pyroxene rims - the annealing would have been a natural consequence of irradiation near the critical temperature for olivine, (5) mixture of the above materials with nebular clinopyroxene and olivine, which escaped nebular processing.

Many chondritic interplanetary dust particles (IDPs) also appear to preserve evidence of an irradiation event, in the form of nm-sized GEMS. The preservation of the fine glassy structures in the Ningqiang dark inclusion, caused by nebular radiation damage, suggests that it was added late into the Ningqiang chondrite, post-dating any parent alteration event. The fayalitic-enrichment of the olivine, and incomplete replacement of some magnetite by fayalitic olivine, and some fayalitic olivine by pyrrhotite must also have occurred in the nebula since it predates the radiation damage event. Survival of the amorphous ferromagnesian materials and carbon, *as well as their pre-irradiation precursor mineralogy*, requires that the entire subsequent history of the Ningqiang dark inclusion occurred under conditions of low temperature and low humidity. Thus, this material represents one of the most pristine nebular samples available for study in the lab today, more primitive than even the bulk of anhydrous chondritic IDPs.

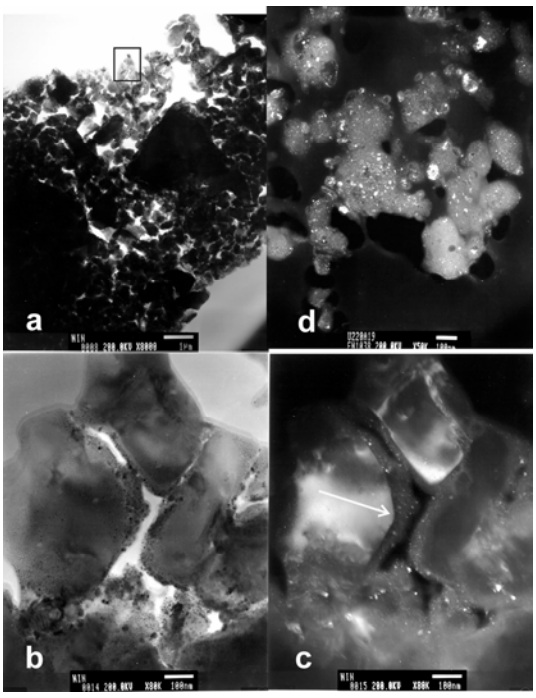

Figure 1: TEM images of Ningqiang dark inclusion (a-c) and a chondritic IDP (d). (a&b) Light-field and (c) dark-field TEM images of euhedral olivine crystals rimmed with amorphous mafic silicate material (dark and arrowed in the dark-field image) and embedded spinels and pyrrhotite (white spots in dark-field). Images (b) and (c) are from the outlined area in (a). (d) Dark field TEM image of GEMS in an anhydrous chondritic interplanetary dust particle. Compare the texture of the GEMS with the amorphous rims in (c), these images are at the same scale. Scale bars measure 100 nm. Image of IDP courtesy of J. Bradley.

Kaidun Meteorite: The Kaidun meteorite contains just about everything, so appears a logical place to search for parent materials from the home of the hydrous chondritic IDPs [5]. One particular lithology we describe here is present in most sections of Kaidun [5], where it was described as a new type of C2 chondrite. This C2 material is petrographically and mineralogically distinct from known C2 meteorites, and consists mainly of a dense assemblage of saponite, serpentine, olivine, ortho- and clinopyroxene, Ca-Mg-Fe carbonates, pyrrhotite, pentlandite, magnetite, and sundry other accessory minerals. In practically all examples this lithology is very dense, and so we never really considered a connection with IDPs. However, in one Kaidun sample we have observed this lithology grading into exceedingly porous (*up to ~50%*) regions, often with rounded pores (see Figure 2). The pores must have originally contained some lost phase, which we suggest was predominantly water ice.

The lithology found in Kaidun appears to be mineralogically and petrographically identical with the bulk of the hydrous chondritic IDPs. Such a link could be tested by an examination of O and N isotopes, which we intend to perform. We suggest that the pores in this material were originally filled by ices, which sublimated away (probably) on the Kaidun parent asteroid. The original home of such material would probably be on C, P or D asteroids, especially the hydrated C-class (Ch) asteroids.

Conclusions: The observations do not permit definite conclusions, but do suggest that existing primitive chondritic regolith breccias do carry samples from the parent bodies of IDPs, in some cases samples that are both larger and more pristine than those we recover from the stratosphere.

References: [1] Zolensky and Barrett (1994) *Meteoritics* ***29***, 616-620; [2] Corrigan et al. (1997) *MAPS* **32**, 509-515; [3] Bradley and Brownlee (1991) *Science* **251**, 549-552; [4] Gounelle et al. (2003) *GCA* **67**, 507-527; [5] Zolensky et al. (2003) *MAPS* **38**,305-322; [6] Zolensky and Ivanov (2003) *Chemie de Erde* **63**, 185-246.

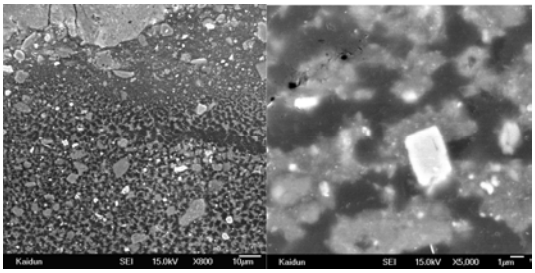

Figure 2: SEI images of the porous Kaidun C2 lithology, (left) grading into the massive lithology above, and (right) higher mag.